

THESIS

PROCESSING AND CHARACTERIZATION  
OF THIN CADMIUM TELLURIDE SOLAR CELLS

Submitted by

Anna Wojtowicz

Department of Physics

In partial fulfillment of the requirements

For the Degree of Master of Science

Colorado State University

Fort Collins, Colorado

Fall 2017

Master's Committee:

Advisor: James R. Sites

W. S. Sampath  
José de la Venta

Copyright by Anna Wojtowicz 2017

All Rights Reserved

# ABSTRACT

## PROCESSING AND CHARACTERIZATION OF THIN CADMIUM TELLURIDE SOLAR CELLS

Cadmium telluride (CdTe) has the highest theoretical limit to conversion efficiency of single-junction photovoltaic (PV) technologies today. However, despite a maximum theoretical open-circuit voltage of 1.20 V, record devices have historically had voltages pinned around only 900 mV. Voltage losses due to high recombination rates remains to be the most complex hurdle to CdTe technology today, and the subject of on-going research in the physics PV group at Colorado State University. In this work, an ultrathin CdTe device architecture is proposed in an effort to reduce bulk recombination and boost voltages. By thinning the CdTe layer, a device's internal electric field extends fully towards the back contact. This quickly separates electrons-hole pairs throughout the bulk of the device and reduces overall recombination. Despite this advantage, very thin CdTe layers also present a unique set of optical and electrical challenges which result in performance losses not as prevalent in thicker devices.

When fabricating CdTe solar cells, post-deposition treatments applied to the absorber layer are a critical step for achieving high efficiency devices. Exposure of the polycrystalline CdTe film to a chlorine species encourages the passivation of dangling bonds and larger grain formation, while copper-doping improves device uniformity and voltages. This work focuses on experiments conducted via close-space sublimation to optimize CdCl<sub>2</sub> and CuCl treatments for thin CdTe solar cells. Sweeps of both exposure and anneal time were performed for both post-deposition treatments on CdTe devices with 1.0 μm absorber layers. The results demonstrate that thin CdTe devices require substantially less post-deposition processing than standard thicker devices as expected. Additionally, the effects of CdTe growth

temperature on thin devices is briefly investigated. The results suggest that higher growth temperatures lead to both electrical and stoichiometric changes in CdTe closely associated with lower carrier lifetimes and poorer overall performance.

## ACKNOWLEDGMENTS

First and foremost, I'd like to thank my advisor, James Sites, for his patience and guidance throughout my research. Jim has been both a wonderful mentor and excellent resource as a subject matter expert. Thank you also to my advisory committee, W. S. Sampath and José de la Venta, for reviewing my work and making insightful contributions. I'd additionally like to thank Dr. Sampath for use of his fabrication lab and Kevan Cameron for system support.

I must also extend a very special thank you to Jennifer Drayton and Alex Huss whom I worked closely with for the past year and contributed hundreds of hours of device fabrication and measurements contained in this thesis. I also owe my gratitude to the many helpful discussions with other colleagues over the course of my research: Andrew Moore, Ramesh Pandey, John Raguse, Jason Kephart, Drew Swanson and others.

Lastly, I'd like to thank my parents, for without their sacrifices I never would have had this opportunity in life.

## TABLE OF CONTENTS

Abstract . . . . .	ii
Acknowledgments . . . . .	iv
List of Tables . . . . .	vi
List of Figures. . . . .	vii
1 Introduction . . . . .	1
1.1 Solar Energy . . . . .	1
1.2 Background . . . . .	2
1.2.1 Solar Irradiation . . . . .	2
1.2.2 Physics of Solar Cells . . . . .	3
2 Cadmium Telluride Solar Cells . . . . .	8
2.1 Limits to Efficiency . . . . .	8
2.2 Fabrication Process . . . . .	12
2.3 Thin Absorber Design . . . . .	14
3 Solar Cell Characterization . . . . .	17
3.1 Current Density-Voltage . . . . .	17
3.2 Quantum Efficiency . . . . .	20
3.3 Electroluminescence . . . . .	22
3.4 Performance Loss Analysis . . . . .	25
3.4.1 Current Losses . . . . .	25
3.4.2 Fill Factor Losses . . . . .	31
4 Processing Optimization . . . . .	36
4.1 CdCl <sub>2</sub> Passivation . . . . .	37
4.1.1 CdCl <sub>2</sub> Dose Sweep . . . . .	37
4.1.2 CdCl <sub>2</sub> Anneal Sweep . . . . .	40
4.2 Cu-doping . . . . .	42
4.2.1 CuCl Dose Sweep . . . . .	42
4.2.2 CuCl Anneal Sweep . . . . .	46
5 Effects of Cadmium Telluride Growth Temperature. . . . .	50
5.1 Voltage-dependent Collection . . . . .	50
5.2 CdCl <sub>2</sub> Passivation . . . . .	54
6 Conclusions . . . . .	56
Bibliography. . . . .	59

## LIST OF TABLES

2.1	Maximum limits to CdTe performance over an ambient temperature range of 60°C	11
2.2	SEM and C-V results showing the physical and electrical widths of thin CdTe cells	14
3.1	Maximum theoretical current and current losses for two thin CdTe devices . . .	28
3.2	Relative fill factor losses calculated for two CdTe devices with different absorber thicknesses . . . . .	33
3.3	J-V parameters for two CdTe devices with different absorber thicknesses . . . .	34
4.1	J-V metrics of best devices as a function of CdCl <sub>2</sub> anneal time . . . . .	40
5.1	Average J-V metrics for the devices of comparable CdTe thickness deposited at standard and high temperatures . . . . .	50

## LIST OF FIGURES

1.1	Solar irradiation spectra of AM0 and AM1.5G . . . . .	3
1.2	Diagram of a $p$ - $n$ junction with charge density, electric field and built-in voltage	4
1.3	Band diagram of a thin CdTe solar cell under forward bias . . . . .	5
1.4	The equivalent circuit of a thin-film solar cell . . . . .	6
1.5	J-V curves illustrating $V_{OC}$ , $J_{SC}$ and fill factor . . . . .	7
2.1	The results of the Shockley-Queisser limit at standard testing conditions . . . . .	10
2.2	The effects of different ambient temperatures on the the Shockley-Queisser limit	11
2.3	Substrate and superstrate cell structures . . . . .	12
2.4	C-V results of thin CdTe devices with absorbers ranging 0.5 $\mu\text{m}$ to 1.3 $\mu\text{m}$ in thickness . . . . .	15
2.5	Basic 1.0 $\mu\text{m}$ CdTe device superstrate structure used throughout this work . . . . .	15
3.1	The four J-V plots used to characterize parasitic losses in thin-film solar cells . . . . .	18
3.2	QE and 1-R curves of a thin CdTe device . . . . .	21
3.3	QE and 1-R curves for CdTe devices with absorber thicknesses ranging from 0.6 $\mu\text{m}$ to 1.2 $\mu\text{m}$ . . . . .	22
3.4	EL images of thin CdTe devices demonstrating uniformity, non-uniformity and defects . . . . .	23
3.5	Several solar cells illustrating the reciprocity relationship between $V_{OC}$ and EL intensity . . . . .	24
3.6	Front-surface reflection in a MZO/CdTe solar cell . . . . .	25
3.7	Current losses for 0.6 $\mu\text{m}$ and 1.0 $\mu\text{m}$ CdTe devices . . . . .	29
3.8	TRPL results for devices with CdTe absorbers ranging 0.4 $\mu\text{m}$ to 1.2 $\mu\text{m}$ thick . . . . .	30
3.9	Absolute fill factor losses calculated for two CdTe devices made at CSU with different absorber thicknesses . . . . .	35
4.1	J-V curves for best devices over a range of CdCl <sub>2</sub> doses . . . . .	37
4.2	J-V metrics as a function of CdCl <sub>2</sub> dose time for 1.0- $\mu\text{m}$ CdTe devices . . . . .	38
4.3	Efficiency as a function of CdCl <sub>2</sub> dose time for CdTe thicknesses ranging 0.6 $\mu\text{m}$ to 1.2 $\mu\text{m}$ . . . . .	39
4.4	J-V metrics as a function of CdCl <sub>2</sub> anneal time for 1.0- $\mu\text{m}$ CdTe devices . . . . .	41
4.5	J-V metrics as a function of CuCl dose time for 1.0- $\mu\text{m}$ CdTe devices . . . . .	43
4.6	The effects of carrier lifetime and back surface doping on 4.0- $\mu\text{m}$ CdTe devices modeled with non-uniform carrier lifetimes throughout the absorber . . . . .	44
4.7	EL images as a function of CuCl dose time . . . . .	45
4.8	J-V curves for 1.0- $\mu\text{m}$ CdTe devices treated with 2, 6 10 seconds CuCl exposure followed by 35-220 seconds annealing . . . . .	46
4.9	J-V metrics as a function of both CuCl dose and anneal time for 1.0- $\mu\text{m}$ CdTe devices . . . . .	48
4.10	Fill factor losses as a function of CuCl anneal time . . . . .	49

5.1	J-V curves for thin CdTe devices with CdTe deposited at standard and high temperatures . . . . .	51
5.2	Comparison of voltage-dependent collection in devices with CdTe deposited at standard and high temperatures . . . . .	52
5.3	TRPL results for devices with CdTe deposited at standard and high temperatures	53
5.4	J-V metrics as a function of CdCl <sub>2</sub> dose for devices with 1.0- $\mu$ m CdTe deposited at high temperature . . . . .	54
5.5	J-V metrics as a function of CdCl <sub>2</sub> dose for best devices with CdTe deposited at standard and high temperatures . . . . .	55

# Chapter 1

## INTRODUCTION

For much of the past century, Earth's atmospheric carbon dioxide (CO<sub>2</sub>) levels have been climbing at an unprecedented rate due to worldwide industrialization. In 2015, the global monthly CO<sub>2</sub> average hit 400 parts per million for the first time in recorded history and continues to accelerate [1]. It's estimated that the total world power consumption will reach 30 TW by mid-century, and of that, two-thirds must come from clean energy sources such as solar and wind in order to stabilize CO<sub>2</sub> levels by 2050 [2].

### 1.1 Solar Energy

Today, the solar industry is largely represented by photovoltaic (PV) technology and is predicted to play an increasingly vital role in the major societal shift away from fossil fuels. Between 2010 and 2015, solar energy production increased from 0.1 to 0.9% of the total US power generated [3]. Although solar PV still represents a small fraction of total energy production, it also represents a very rapidly growing market. Between 2000 and 2015, solar PV increased power-generating capacity by a factor of about 57 (from 4 to 227 GW), while other renewable sources increased capacity by only a factor of 9.2 [4]. Additionally, not only is solar PV one of the most rapidly growing renewable energy sources, it's also one of the most inexpensive and already has a Levelized Cost of Energy (\$/MWh) comparable to the traditional combined gas cycle in some parts of the US [5].

While silicon (Si) has largely dominated the worldwide PV market for decades, cadmium telluride (CdTe) is currently the second most common PV technology and the only technology cost-competitive with multicrystalline Si (mc-Si) in utility-scale installations [3, 6]. As a thin-film PV technology, CdTe solar cells are easier, quicker and require less material to manufacture than mc-Si while achieving comparable module performance. This makes CdTe

an attractive alternative to the industry standard, and as a result, one of the fastest growing PV market segments [7].

This work focuses on experimental fabrication and characterization of CdTe solar cells performed at Colorado State University (CSU). Common characterization techniques are presented for assessing solar cell performance, as well as experimental results investigating optimal fabrication parameters for a novel cell architecture. As part of a CSU effort to engineer an ultrathin CdTe solar cell design, this work represents the foundation for fabricating basic heterojunction solar cells with a CdTe layer of approximately 1.0  $\mu\text{m}$ , while also providing insight into issues faced by thin CdTe devices in general.

## 1.2 Background

### 1.2.1 Solar Irradiation

All solar technologies are limited by how much sunlight is available for photovoltaic conversion. The solar irradiance received on Earth's surface is highly variable and dependent on atmospheric effects. A combination of Rayleigh scattering, aerosol and dust scattering, and atmospheric absorption translates to an approximately 30% loss in irradiance by the time light reaches Earth's surface [8]. The path length light must travel has the largest impact on irradiance loss, and the degree of attenuation is the basis for the standardized Air Mass (AM) scale. Air Mass at a particular location is calculated by the equation:

$$AM = \frac{1}{\cos \theta} \tag{1.1}$$

where  $\theta$  is the zenith angle of the sun measured from the surface normal.

Air Mass 0 (AM0) corresponds to a position directly perpendicular to the direction of incident light where  $\theta = 90^\circ$ ; this describes irradiation outside Earth's atmosphere of approximately 1300  $\text{W}/\text{m}^2$  and is considered the standard for extra-terrestrial applications. Air Mass 1 (AM1) occurs when the sun is directly above such that  $\theta = 0^\circ$ ; in this scenario, light

takes the shortest path through the atmosphere experiencing minimal attenuation. While AM1 can be used for equatorial applications, the majority of developed countries employing solar technologies lie in the mid-latitudes. As such, the terrestrial standard used in research and industry is AM1.5G corresponding to  $\theta = 48.2^\circ$  and an irradiation of approximately  $1000 \text{ W/m}^2$ , where ‘G’ denotes both direct and diffuse components of sunlight.

Fig 1.1 illustrates the overall difference in spectral power between AM0 and AM1.5G, in addition to highlighting absorption bands due to ozone ( $\text{O}_3$ ), water vapor ( $\text{H}_2\text{O}$ ) and carbon dioxide ( $\text{CO}_2$ ) in the atmosphere.

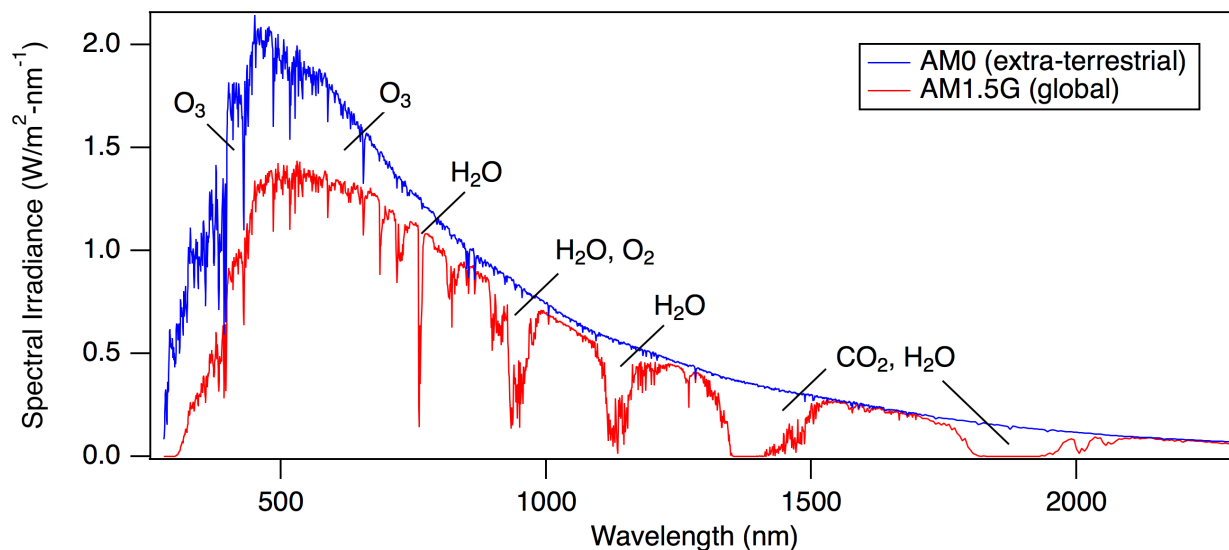


Fig. 1.1: Solar irradiation spectra of AM0 and AM1.5G with regions of atmospheric absorption indicated.

### 1.2.2 Physics of Solar Cells

The basic operation of a solar cell relies on the formation of a  $p$ - $n$  junction to collect photogenerated carriers. When bringing  $p$ - and  $n$ -type materials together, dopant atoms near the junction become ionized creating a region depleted of carriers. Excess holes near the junction diffuse from from the  $p$ -type side to the  $n$ -type leaving negatively-charged acceptor atoms behind, while similarly, excess electrons diffuse from the  $n$ -type side to  $p$ -type leaving positively-charged donor atoms behind [9].

This diffusion process cannot continue indefinitely due to Coulomb interaction, and eventually a state of charge equilibrium is reached. What remains is a carrier-depleted region about the junction with ionized dopant and acceptor atoms on each side inducing a built-in voltage and internal electric field. This region of the device is known as the space-charge region (SCR) and is demonstrated in Fig 1.2.

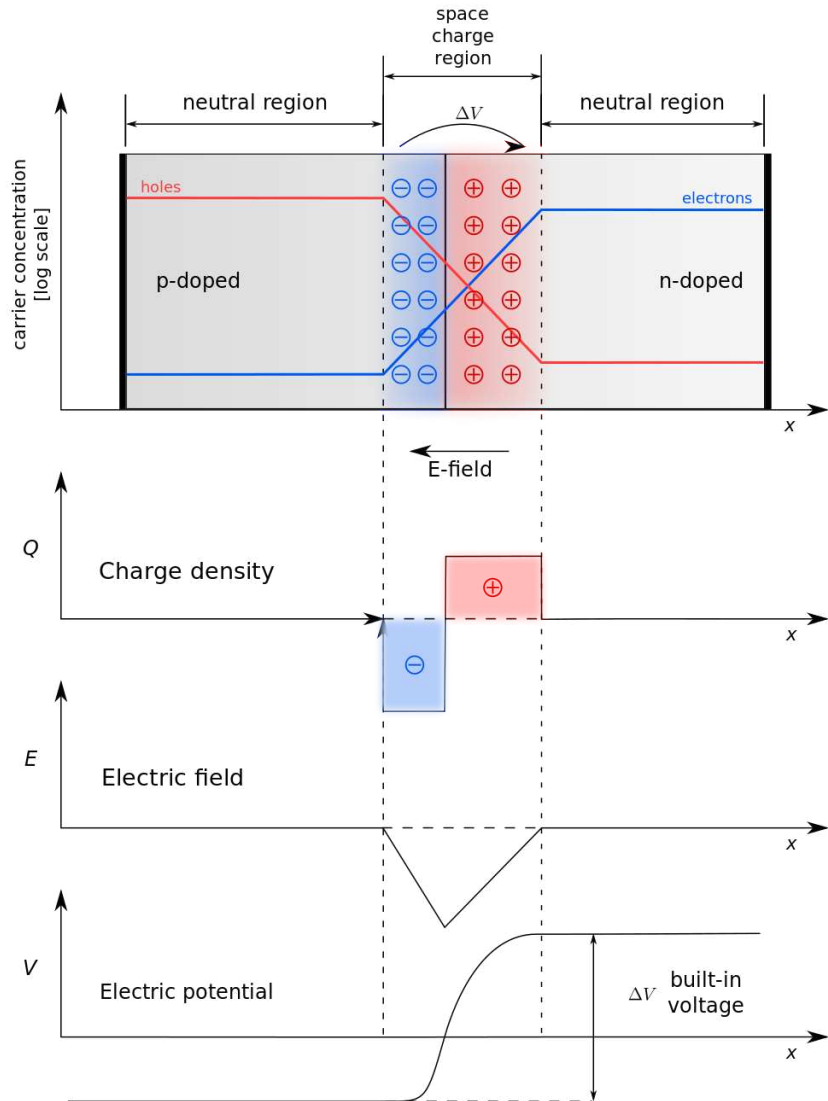


Fig. 1.2: Diagram of a  $p$ - $n$  junction also illustrating associated charge density, electric field and built-in voltage as a function of position. From Ref. [10].

When light is incident on a solar cell such as thin-film CdTe, it passes through a transparent conducting oxide (TCO) front contact before reaching the  $n$ -type material first. The

$n$ -type side of the  $p$ - $n$  junction is selected for its transparency to the visible spectrum and as such is often referred to the *window* layer. Once passing through the window layer, photons with energy equal to or greater than the material bandgap are absorbed in the *absorber* layer where they create electron-hole pairs through the photovoltaic conversion process as shown in Fig. 1.3.

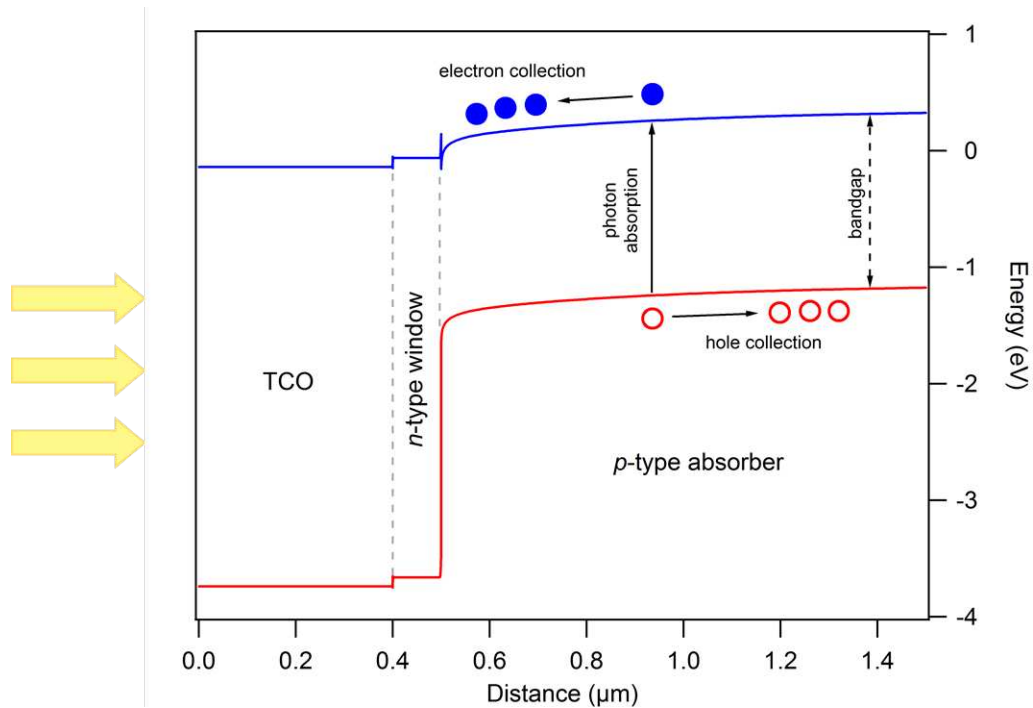


Fig. 1.3: Band diagram of a thin CdTe solar cell with the direction of incident light indicated. The diagram is under forward bias to demonstrate a solar cell’s typical operation.

The presence of an electric field in the SCR quickly separates electron-hole pairs when they are generated, and with the addition of front and back contacts on a device, allows for the carriers to be captured. When the SCR and electric field extend fully throughout the absorber layer to the back contact, the probability of recombination effects decreases. A device with such an electric field is considered *fully-depleted* as all dopant atoms have become ionized. With this in mind, a thinner absorber may become favorable as it requires a smaller electric field to fully deplete the device. This gives thin-film PV technologies like CdTe an advantage over Si which requires relatively thick high-purity absorbers to achieve comparable performance.

Since the operation of solar cells requires a  $p$ - $n$  junction, solar cells are modeled as diodes and thusly their current density-voltage (J-V) characteristics follow the ideal diode equation:

$$J = J_0 \left[ \exp\left(\frac{qV}{kT}\right) - 1 \right] - J_L \quad (1.2)$$

where  $q$  is the elementary charge,  $k$  is the Boltzmann constant,  $T$  is the absolute temperature,  $J_L$  is the light-generated current and  $J_0$  is the reverse-saturation current density. When the applied bias is negative by a factor of a few  $kT/q$ , then the current density becomes independent of voltage resulting in the reverse-saturation current density term,  $J_0$ .

However, solar cells suffer from parasitic losses not accounted for by the ideal diode equation. These losses include series and shunt resistance which occur in series and parallel with the primary diode, respectively. Fig. 1.4 shows the equivalent circuit of a thin-film solar cell.

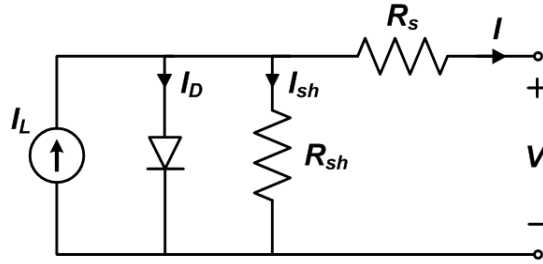


Fig. 1.4: The equivalent circuit of a thin-film solar cell.  $I_L$  is the light-generated current, while  $R_s$  and  $R_{sh}$  are the series and shunt resistance, respectively. From Ref. [11].

Adapting the ideal diode equation for the circuit depicted in Fig. 1.4 leads to the J-V characteristic equation:

$$J = J_0 \exp\left[\frac{q}{AkT}(V - RJ)\right] + GV - J_L \quad (1.3)$$

where  $A$  is the ideality factor of the diode,  $R$  is the series resistance and  $G$  the shunt conductance. A method for extracting these parameters from device measurements will be covered in Section 3.1.

Plotting the current density as a function of voltage leads to solar cell's J-V response curve where three useful parameters are extracted from the fourth quadrant: short-circuit current density ( $J_{SC}$ ), open-circuit voltage ( $V_{OC}$ ), and fill factor ( $FF$ ).  $J_{SC}$  occurs where the applied bias is 0,  $V_{OC}$  occurs where the current density is 0, and fill factor is a measure of a device's relative deviation from ideal maximum power such that  $P_{ideal} = J_{SC} V_{OC}$ . These three metrics along with  $J_{MP}$  and  $V_{MP}$ , the current density and voltage at the device's actual maximum power point, are illustrated in Fig. 1.5.

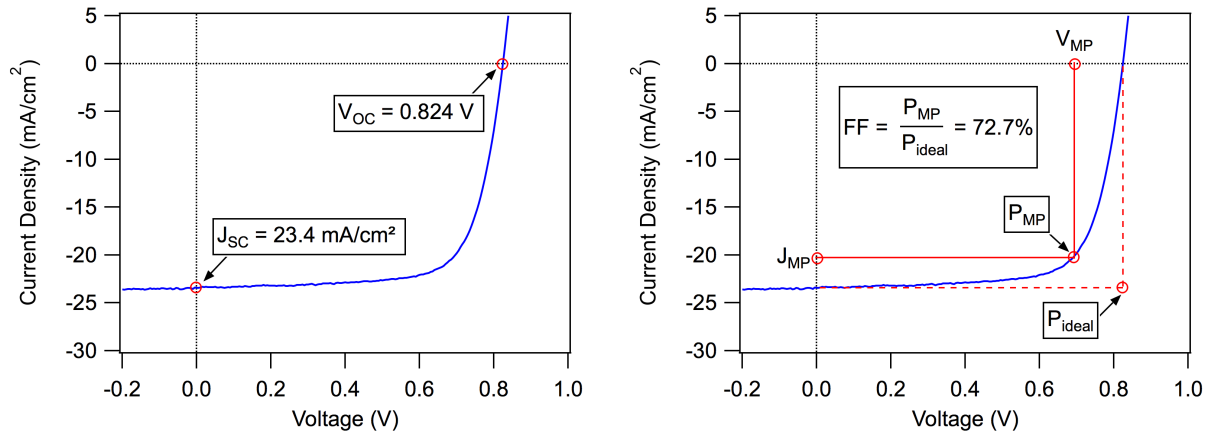


Fig. 1.5: J-V curves illustrating the performance metrics obtained from the ‘power’ quadrant:  $J_{SC}$ ,  $V_{OC}$  and calculated fill factor.

Once the basic J-V metrics are known, one can calculate the device's overall conversion efficiency using the equation:

$$\eta = \frac{P_{ideal} FF}{P_{in}} = \frac{J_{SC} V_{OC} FF}{P_{in}} \quad (1.4)$$

where  $P_{in} = 100 \text{ mW/cm}^2$  from standardized testing conditions.

# Chapter 2

## CADMIUM TELLURIDE SOLAR CELLS

Cadmium telluride (CdTe) is a II-VI direct-bandgap semiconductor and has optical properties well-aligned with the solar spectrum received on Earth's surface. A bandgap of 1.49 eV ( $\lambda \sim 832$  nm) means CdTe is capable of absorbing a large portion of the AM1.5 spectrum. Its absorption range coupled with a high absorption coefficient ( $> 10^5$  cm<sup>-1</sup>) means 99% of incident light is absorbed within 2  $\mu$ m of CdTe film, making it an attractive thin-film PV technology [12].

### 2.1 Limits to Efficiency

The thermodynamic limit to single  $p$ - $n$  junction conversion efficiency was originally developed by Shockley and Queisser in 1961 and remains fundamental to benchmarking PV technology today [13]. The Shockley-Queisser (S-Q) limit states that blackbody radiation from inefficient photoconversion ultimately limits the performance of single-junction solar cells to a well-defined value based on the absorber bandgap and illumination spectrum. Any photon with energy above a material's bandgap generates at most one electron-hole pair with the remainder of energy converted to phonon vibrations that result in recombination.

Assuming one photon with wavelength  $\leq \lambda_G$  produces one electron-hole pair in the absorber material, the maximum theoretical short-circuit current density ( $J_{SC}$ ) of a cell is calculated as

$$J_{SC, ideal} = q \int_0^{\lambda_G} N(\lambda) d\lambda \quad (2.1)$$

where  $q$  is the elementary charge and  $N(\lambda)$  is spectral photon flux density such that  $N(\lambda) = \lambda P(\lambda)/hc$ , with  $P(\lambda)$  being the spectral irradiance from the sun. Assuming the device is a perfect blackbody with no non-radiative recombination, the ideal open-circuit voltage ( $V_{OC}$ )

is calculated as

$$V_{OC, ideal} = \frac{kT}{q} \ln \left( \frac{J_{SC}}{J_0} + 1 \right) = \frac{kT}{q} \ln \left( \frac{\int_0^{\lambda_G} N(\lambda) d\lambda}{\int_0^{\lambda_G} \phi_{BB}(\lambda) d\lambda} + 1 \right) \quad (2.2)$$

where  $\phi_{BB}$  is the spectral density of blackbody emissivity such that  $\phi_{BB} = \lambda F(\lambda)/hc$ .  $F(\lambda)$  is the spectral irradiance from black body radiation as defined by Planck's radiation law:

$$F(\lambda) = \frac{2\pi hc^2}{\lambda^5 (\exp[\frac{E_G}{kT}] - 1)}. \quad (2.3)$$

The fill factor of a J-V curve is calculated by maximizing  $J \times V$  which leads to a transcendental equation. An analytic solution was developed such that the ideal fill factor can accurately estimated to about four significant digits for  $\nu_{OC} > 10$  [8]:

$$FF_{ideal} = \frac{\nu_{OC} - \ln(\nu_{OC} + 0.72)}{\nu_{OC} + 1} \quad (2.4)$$

where  $\nu_{OC}$  is the thermal-voltage normalized  $V_{OC}$ :

$$\nu_{OC} = \frac{q}{kT} V_{OC}. \quad (2.5)$$

Lastly, the conversion efficiency can be calculated by:

$$\eta = \frac{P_{max}}{P_{sun}} = \frac{J_{SC} V_{OC} FF}{\int_0^{\infty} P(\lambda) d\lambda}. \quad (2.6)$$

The results of the S-Q limit are shown in Fig. 2.1. As the bandgap widens,  $J_{SC}$  decreases, while conversely,  $V_{OC}$  and fill factor increase. The implications of the S-Q limit results in a maximum theoretical efficiency of  $\eta = 33.16\%$  ( $E_G = 1.34$  eV) for terrestrial applications [14]. Also indicated in dashed lines are the bandgaps of such an ideal material along with CdTe, at 1.34 eV and 1.49 eV respectively. The curves were calculated at standard testing conditions (AM1.5G, 100 mW/cm<sup>2</sup>, 25°C), and as such, fill factor does not reach unity.

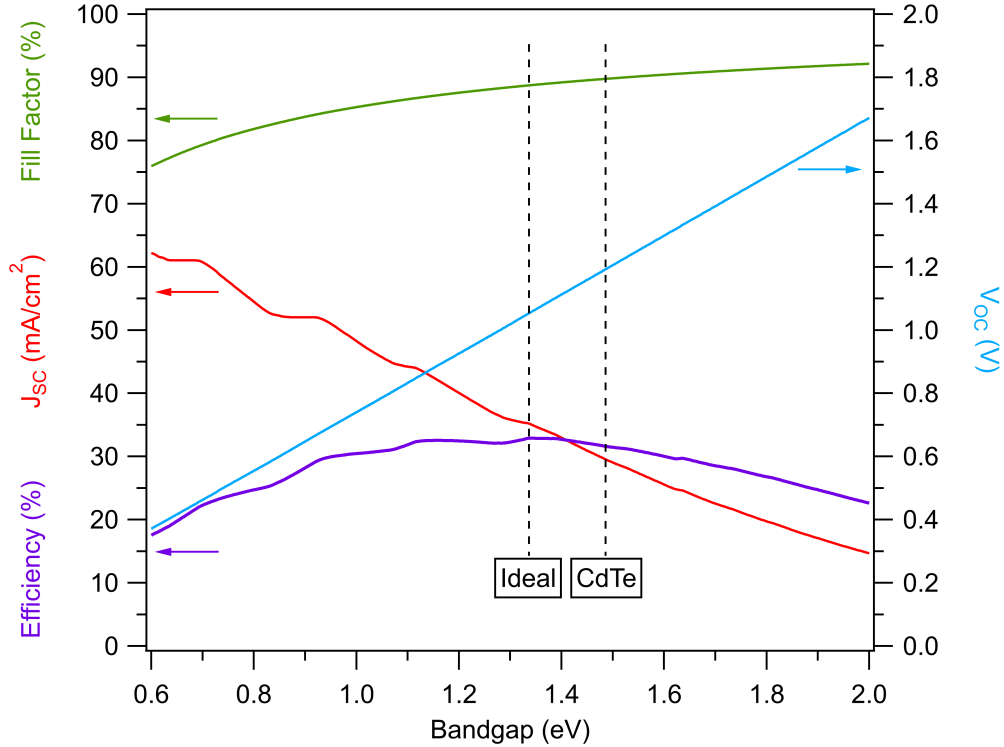


Fig. 2.1: The results of the Shockley-Queisser limit at standard testing conditions with the bandgaps of CdTe (1.49 eV) and an ideal absorber (1.34 eV) material indicated. Based on Ref. [15].

However, the S-Q limit assumes an ambient temperature of 25°C, which is likely an unrealistic representation of solar panels in the field. The effects of temperature on the S-Q limit can be seen in Fig. 2.2. Larger bandgap materials are generally less susceptible to decreases in performance at high ambient temperatures than lower bandgap materials. In particular, ideal Si cells would experience an approximate 3.2% (absolute) decrease in efficiency when raising the temperature from 0 to 60°C, while CdTe experiences only a 2.4% drop over the same temperature range. This trend in temperature, originally published by Ref. [15] and reproduced here, suggests slightly higher bandgap materials like CdTe may be advantageous over Si in warmer climates where utility-scale solar is more likely to be deployed.

A table of temperature-dependent CdTe performance metrics is given in Table 2.1.  $J_{SC}$  seems to remain unaffected by a 60°C temperature difference while  $V_{OC}$  appears most sus-

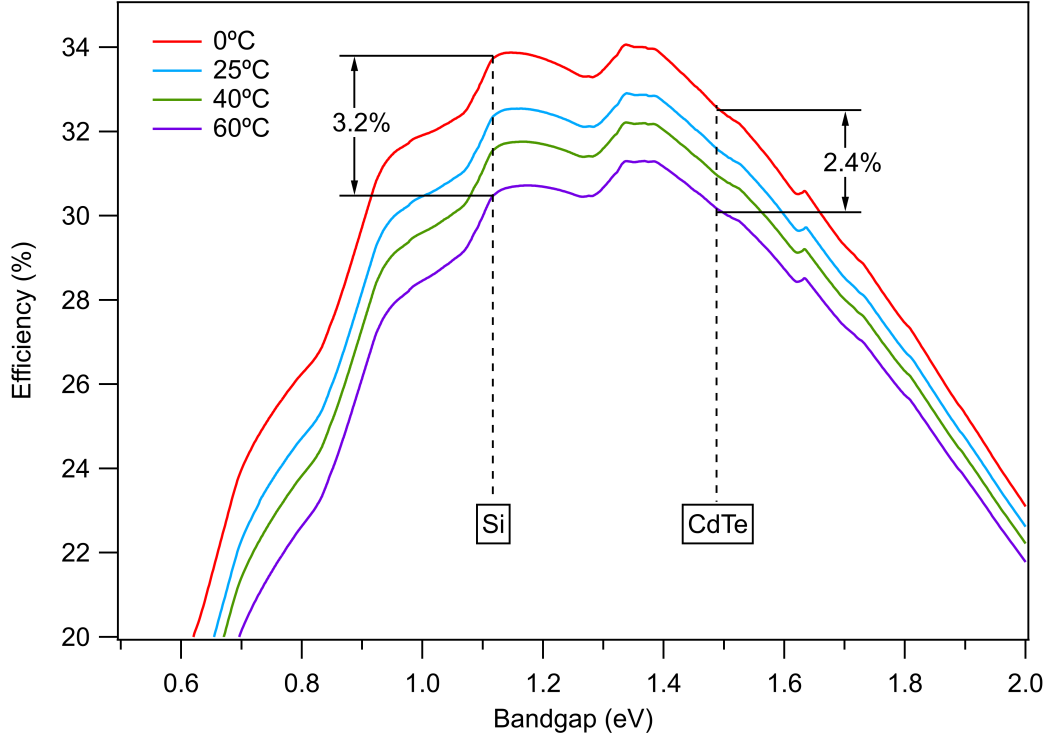


Fig. 2.2: The effects of different ambient temperatures on the the Shockley-Queisser limit. Silicon experiences a greater decrease in ideal performance than CdTe at higher temperatures. Based on Ref. [15].

ceptible to warmer temperatures. Over the given temperature range,  $V_{OC}$  spans 70 mV while the fill factor only changes by only about 2% (absolute). On the assumption that radiative recombination is mediated by phonon vibrations, it confirms that the  $V_{OC}$  should be most impacted by warmer temperatures. The net result is a maximum limit to CdTe efficiency ranging from 30.1 to 32.5% over a temperature range of 60°C which one can reasonably expect modules to experience in the field.

Table 2.1: Maximum limits to CdTe performance over an ambient temperature range of 60°C predicted by the Shockley-Queisser limit.

T (°C)	$J_{SC}$ (mA/cm <sup>2</sup> )	$V_{OC}$ (V)	FF (%)	$\eta$ (%)
0	29.3	1.23	90.7	32.5
25	29.3	1.20	89.8	31.5
40	29.3	1.18	89.3	30.9
60	29.3	1.16	88.6	30.1

## 2.2 Fabrication Process

Thin-film solar cells can be made in one of two configurations: *substrate* or *superstrate* as illustrated in Fig. 2.3. A *substrate* configuration involves depositing the thin-films onto a piece of glass from back-to-front where a transparent conducting oxide (TCO) layer is deposited last. A *superstrate* configuration is the reverse, whereas films are deposited front-to-back so that the back contact is deposited last. In the latter configuration, incident photons must also pass through the piece of glass first before entering the device. Despite this additional layer, CdTe devices have historically found most success in *superstrate* configurations.

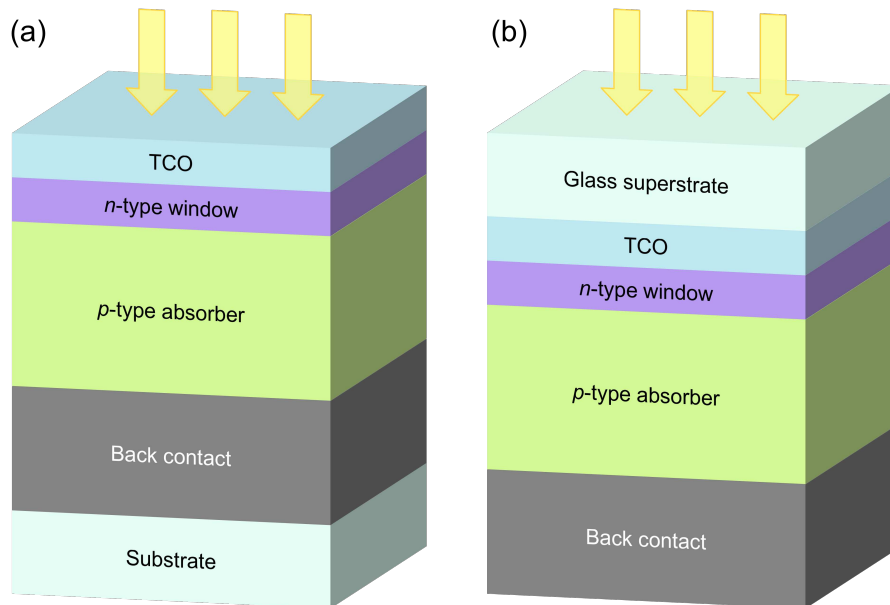


Fig. 2.3: (a) Substrate cell structure, and (b) superstrate cell structure with the direction of incident light indicated.

To fully utilize CdTe's ideal range of optical absorption in a heterojunction structure, it's necessary to be paired with a highly transparent, wide bandgap material. Since nearly all such known materials are *n*-type, the CdTe absorber must be *p*-type. Additional considerations must also be given when selecting the window layer; lattice mismatch and the potential for diffusion must both be minimized. The latter can be addressed by selecting a column II cation (Zn, Cd, Hg) to promote long term stability. As a result, cadmium sulfide (CdS)

has found considerable success as a  $n$ -type window layer in the highest performing CdTe devices to date [7]. Although CdS has proven itself a suitable match for CdTe, it suffers from absorption at lower wavelengths that limits CdTe cells from reaching their potential performance. Other window layers that have been investigated include cadmium selenide (CdSe), cadmium zinc sulfide (CdZnS), zinc selenide (ZnSe), zinc oxide (ZnO), and the window layer used this work, magnesium zinc oxide (MgZnO).

Improvements made to the fabrication process during the 80s and 90s established a foundation for creating high quality CdTe devices; this included optimized processing temperatures, the addition of low-resistance back contact layers and most importantly, post-deposition treatments [12]. Common post-deposition treatments used today include: cadmium-chloride ( $\text{CdCl}_2$ ) passivation and copper (Cu) doping.

The exposure of CdTe to a chlorine species has been key for achieving high efficiency devices. In doing so, followed by an annealing process, exposure to the  $\text{CdCl}_2$  treatment encourages recrystallization of the absorber material leading to grain coalescence, passivation of dangling bonds, and improved bulk electronic properties [16]. This occurs primarily by filling Te vacancies near grain boundaries with Cl atoms, leading to  $p$ -type grains with  $n$ -type grain boundaries [17]. A commonly used material is the hygroscopic salt cadmium chloride, but other forms of chlorine are also effective.

Due to the high work function of CdTe, formation of an ohmic contact with a metal at the back of a device has not been successful. Thus, Cu-doping is a widely used method to encourage formation of a  $p$ -rich pseudo-ohmic gradient at the back of the CdTe film. However, CdTe itself is not easily doped with impurity atoms; experimental results suggest that through a chemical reaction process, copper exposure followed by an anneal produces something more akin to a new bulk phase contact material such as  $\text{Cu}_{2-x}\text{Te}_x$  [18]. Care must be taken as to not over-dope when forming the  $\text{Cu}_{2-x}\text{Te}_x$  contact; excess copper is known to increase recombination and migrate through the absorber to the  $p$ - $n$  junction by way of grain boundary diffusion, leading to long-term instability of devices [19].

## 2.3 Thin Absorber Design

While CdTe is nearly optimal for terrestrial PV applications in many ways, it is not without its limitations. One of the largest limitations of CdTe technology high recombination rates due to low carrier lifetimes. Until this issue can be addressed, CdTe will continue struggling to exceed voltages of 1 V and remains unable to realize its potential as one of the highest theoretical performing single-junction PV technologies.

High bulk recombination rates in today’s CdTe devices can be potentially addressed by a novel cell architecture. In principle, a thinner absorber will lead to a more fully-depleted device. The extension of the internal electric field throughout the device will create separate conduction pathways for both electrons and holes in the bulk of the CdTe, thus decreasing the probability of bulk recombination. Additionally, by extending the depletion width to the back contact, carrier diffusion and thus dark saturation current are minimized by a lack of field-free regions. Preliminary capacitance-voltage (C-V) and scanning electron microscope (SEM) measurements show that thin CdTe absorbers are capable of being fully or near fully-depleted, illustrated in Table 2.2 and Fig. 2.4.

Table 2.2: SEM and C-V results showing the physical and electrical widths of thin CdTe cells. Thin CdTe cells are capable of being fully or near fully-depleted while unbiased.

Physical width ( $\mu\text{m}$ )	Electrical width ( $\mu\text{m}$ )	Depletion (%)
0.51	0.51	100
0.69	0.65	94
1.04	0.92	88
1.30	0.94	72

The proposed basic cell architecture is shown in Fig. 2.5. All experimental details described in future chapters utilize this same device structure and processing routines unless otherwise noted. Devices are fabricated on a commercial superstrate of 3.2-mm soda-lime glass coated with a 400-nm TCO layer of  $\text{SnO}_2\text{:F}$  (TEC10 made by Pilkington).  $\text{Mg}_x\text{Zn}_{1-x}\text{O}$  (MZO) has been selected as a window layer for its tunable bandgap ( $x \sim 0.2$ ,  $E_g = 3.6$  eV)

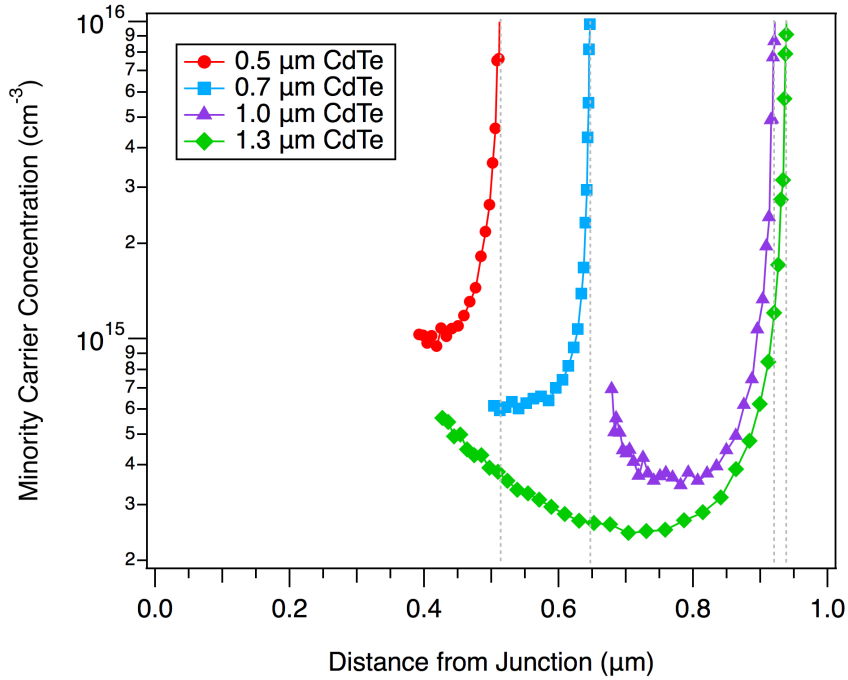


Fig. 2.4: C-V results of thin CdTe devices with absorbers ranging 0.5  $\mu\text{m}$  to 1.3  $\mu\text{m}$  in thickness. Thin CdTe absorbers are fully or near fully-depleted while unbiased.

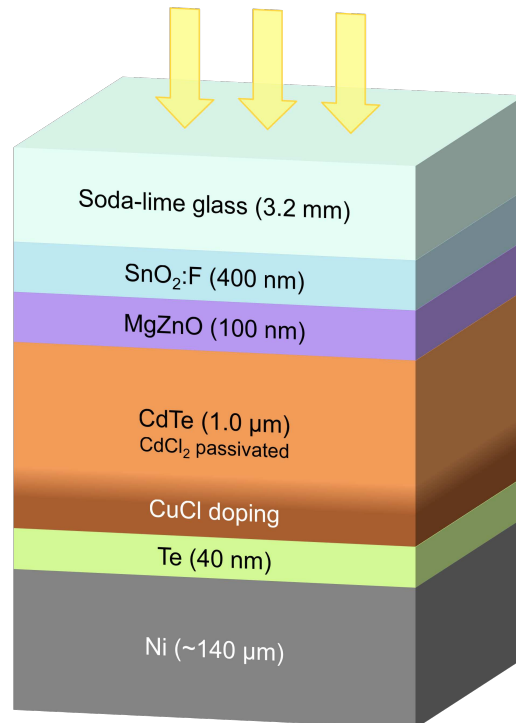


Fig. 2.5: Basic 1.0  $\mu\text{m}$  CdTe device superstrate structure used throughout this work with the direction of incident light indicated.

and superior transparency at lower wavelengths compared to the traditional choice of CdS. A 100-nm MZO window layer is deposited via radio-frequency (RF) sputtering directly onto the TEC10 substrate at room temperature.

CdTe is then deposited at approximately 460°C via close-space sublimation (CSS) by the Advanced Research Deposition System, a single-vacuum deposition system built at CSU [20]. Following CdTe deposition, a CdCl<sub>2</sub> treatment is applied with an annealing process, and the plates are allowed to cool inside the vacuum system before being removed. Any excess CdCl<sub>2</sub> material on the CdTe surface is rinsed using deionized water.

If Cu-doping is desired, the plate is then placed back into the deposition system, heated to 200°C for 75 seconds and then exposed to varying amounts of sublimating CuCl material. An annealing process follows to encourage the formation of the desired CuTe alloy at the back of the absorber. Devices are again allowed to cool in vacuum before removal and then are rinsed of any excess CuCl material with deionized water.

Due to the difficulty in forming ohmic contact with CdTe, a pseudo-ohmic buffer layer of 40-nm Te is evaporated using a Cooke MK VII Evaporator. The Te is helpful in forming a *p*-rich layer at the back of the absorber which reduces the back barrier height. The Te buffer layer is then followed by approximately 140 μm of colloidal Ni. Small-area devices, each measuring 0.60 to 0.65 cm<sup>2</sup> in area, are delineated on the deposited plates.

The use of an expanded-bandgap electron reflector is recommended once fabrication of the baseline structure is optimized, but is not covered in this work. CdMgTe (CMT) is a tunable bandgap alloy which has demonstrated theoretical voltage boosts of up to 200 mV for thin CdTe cells when deposited at the back of the CdTe layer [21]. The slightly wider bandgap (~1.7 eV) at the back creates an energy barrier for electron flow and reduces back surface recombination effects.

# Chapter 3

## SOLAR CELL CHARACTERIZATION

Several common characterization techniques are outlined here for assessing the quality of solar cell performance.

### 3.1 Current Density-Voltage

Current density-voltage (J-V) measurements are a way to evaluate diode-like current behavior both under illumination and in the dark. The most common type of J-V measurement is performed under a standard AM1.5G illumination of 100 mW/cm<sup>2</sup> at 25°C while voltage is swept and current density response is measured. All J-V data presented in this work were tested at these conditions using a Solar Light Co. xenon arc lamp solar simulator and neutral density filter, with Keithley 2401 sourcemeters in a 4-lead configuration.

Section 1.2.2 outlined the three basic performance metrics extracted from a J-V curve:  $J_{SC}$ ,  $V_{OC}$ , fill factor and  $\eta$ . While these metrics are useful as a standardized way to compare device performance, a full analysis of CdTe solar cells requires further characterization of the parasitic losses inherent to thin-film PV technologies. This is done by plotting both dark and light J-V curves in the four arrangements shown in Fig. 3.1 [22, 23].

Fig. 3.1(a) shows a normal J-V curve following the thin-film diode equation:

$$J = J_0 \exp\left[\frac{q}{AkT}(V - RJ)\right] + GV - J_L. \quad (3.1)$$

Fig. 3.1(b) shows the shunt conductance term  $g(V) \equiv dJ/dV$  plotted against voltage. When photocurrent is independent of voltage, then  $g(V)$  will be a horizontal line at 0 V and  $J_{SC}$  can be substituted in place of  $J_L$ . However, in practice,  $g(V)$  may have a slight slope equal to  $G$  in Eqn. 3.1, and thus the derivative  $dJ/dV$  can become quite noisy under illumination

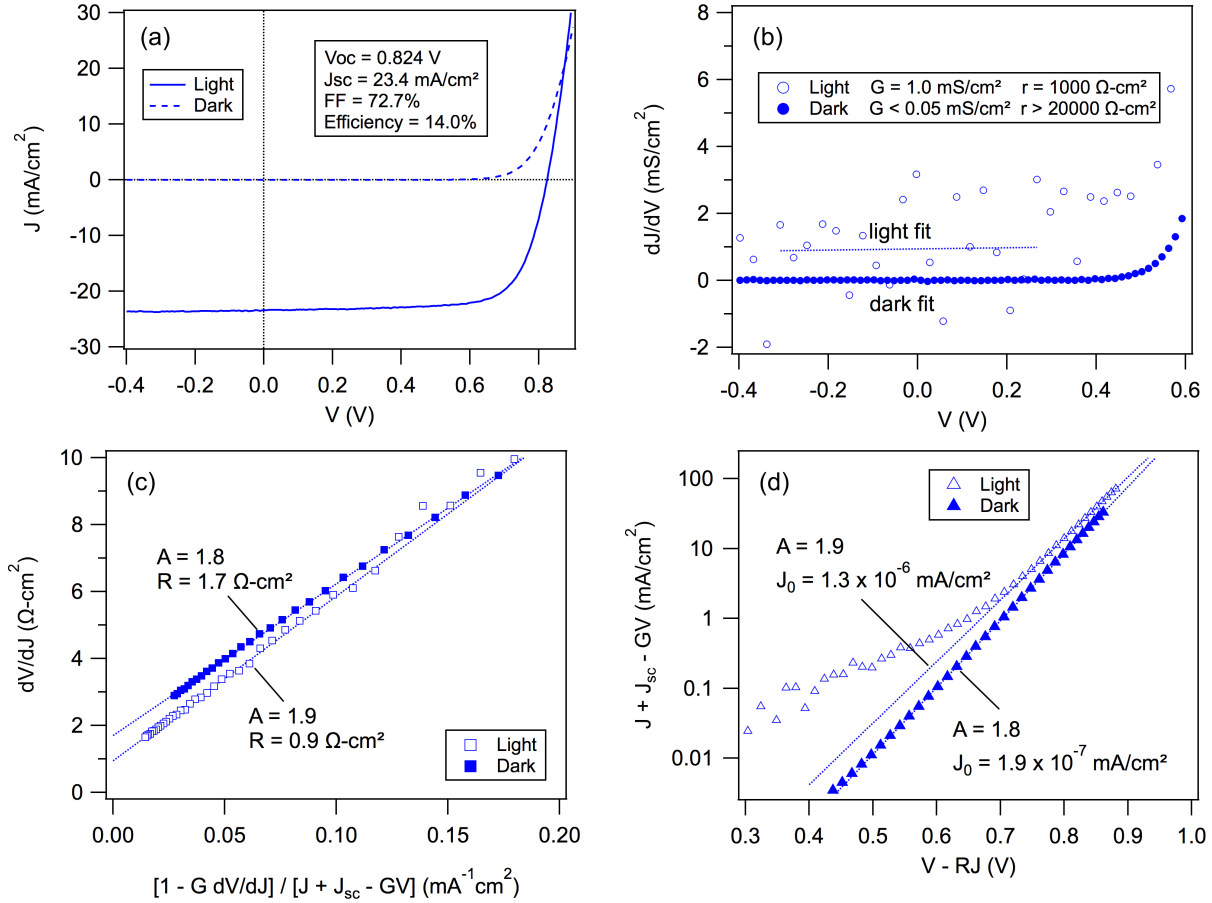


Fig. 3.1: The four J-V plots used to characterize parasitic losses in thin-film solar cells. The data shown is for a device with 1.3- $\mu\text{m}$  CdTe made at CSU without an anti-reflective coating.

creating difficulties in doing a linear regression. In this case, it's useful to first apply a Gaussian filter algorithm to reduce noisiness.

Fig. 3.1(c) shows a plot of the shunt resistance term  $r(J) \equiv dV/dJ$ . By rearranging equation 3.1 for  $r(J)$ , we arrive at the relationship:

$$r(J) \equiv \frac{dV}{dJ} = R + \frac{AkT}{q}(J + J_L)^{-1}. \quad (3.2)$$

In the absence of significant barrier effects, the plot of  $dV/dJ$  against  $(J + J_{SC})^{-1}$  will yield a straight line with slope  $AkT/q$  and an intercept of the series resistance term,  $R$ . However, in the case of non-negligible shunt conductance,  $G$ , the following differential correction to

the abscissa is used:

$$r(J) \equiv \frac{dV}{dJ} = R + \frac{AkT}{q} \left[ \frac{1 - G \left( \frac{dV}{dJ} \right)}{J + J_L - GV} \right] \quad (3.3)$$

and has been shown to reduce uncertainty in fitting  $r(J)$  by a factor of 2-3 for thin-film solar cells [24]. From here, a straight line can be fit with slope  $AkT/q$  and intercept  $R$ . The ideality factor,  $A$ , is extracted and used for comparison in the preceding section.

Fig. 3.1(d) shows a semi-logarithmic plot of the J-V data. Rearranging Equation 3.1 for  $J_0$  produces the expression for forward current:

$$J_F(V) \equiv (J + J_L) = J_0 + \frac{q}{AkT}(V - RJ). \quad (3.4)$$

A linear fit about the  $V_{OC}$  point over 1-2 orders of current magnitude will produce a reliable fit. Again, a correction can be made for the case of non-negligible shunt conductance,  $G$ , to reduce error in linear regression. This time it is made to the ordinate, such that [22]:

$$J_F(V) \equiv (J + J_L - GV) = J_0 + \frac{q}{AkT}(V - RJ) \quad (3.5)$$

where a plot of  $J + J_{SC} - GV$  against  $V - RJ$  will yield a straight line with slope  $q/AkT$  and intercept  $J_0$ . Here, the extracted ideality factor,  $A$ , can be compared to the one produced in the previous plot for agreement.

The data shown in Fig. 3.1 is an example of a high quality cell made at CSU with an MZO window layer and a 1.3  $\mu\text{m}$  CdTe absorber. The device has non-negligible shunt conductance  $G = 1.0 \text{ mS/cm}^2$ , and as such, the previously proposed corrections to the abscissa and ordinate were made. Linear regressions yielded a moderate decrease of series resistance under illumination from  $R = 1.7 \text{ } \Omega\text{-cm}^2$  in dark to  $0.9 \text{ } \Omega\text{-cm}^2$ , and an increase in reverse-saturation current from  $J_0 = 1.9 \times 10^{-7} \text{ mA/cm}^2$  in dark to  $1.3 \times 10^{-6} \text{ mA/cm}^2$ . From plot Fig. 3.1(d) we also see evidence of parasitic effects under illumination that cause the cell's behaviour to deviate from its exponential form.

## 3.2 Quantum Efficiency

External quantum efficiency (EQE) is a measure of a device’s ability to efficiently convert photons to collected carriers and is expressed as a simple ratio:

$$EQE = \frac{\text{carriers/second}}{\text{photons/second}}. \quad (3.6)$$

Ideal conversion would entail collection of one electron-hole pair for each incident photon resulting in a QE ratio of unity; however, solar cells suffer from both external and internal losses resulting in a lower collection probability. QE measurements are typically conducted at  $J_{SC}$ , and when plotted as a function of wavelength, provide useful insight into sources of current losses. External losses include reflection and absorption in the optical stack of window layers preceding the absorber, while internal losses entail incomplete absorption and electrical recombination effects inside the CdTe layer itself.

Fig. 3.2 shows a QE curve for a thin CdTe device made at CSU. A sharp drop of signal at approximately  $\lambda_G = 832$  nm (1.49 eV) is known as the *absorption edge* and is a direct result of the CdTe bandgap, whereas photons with wavelength  $> \lambda_G = 832$  nm (or energy  $< E_G = 1.49$  eV) are not absorbed by the material. It is also useful to plot reflection along with QE data; assuming highly transparent window layers, plotting  $1-R$  serves as a rough indicator that external losses are generally constant across the the visible spectrum.

Most of the difference between the QE and  $1-R$  curves is optical absorption of glass and the TCO. However, different wavelengths of light are also absorbed at different depths in the absorber layer. The absorption depth of light in a semiconductor material is determined by the reciprocal of the material’s absorption coefficient,  $\alpha(\lambda)$ . As CdTe has a high absorption coefficient at low wavelengths, blue light is absorbed at the surface of the absorber layer whereas red light tends to be absorbed towards the back.

As illustrated in Fig. 3.2, the QE curve slopes gradually downwards in the red wavelengths before the absorption edge, suggesting less collection from photons penetrating more deeply.

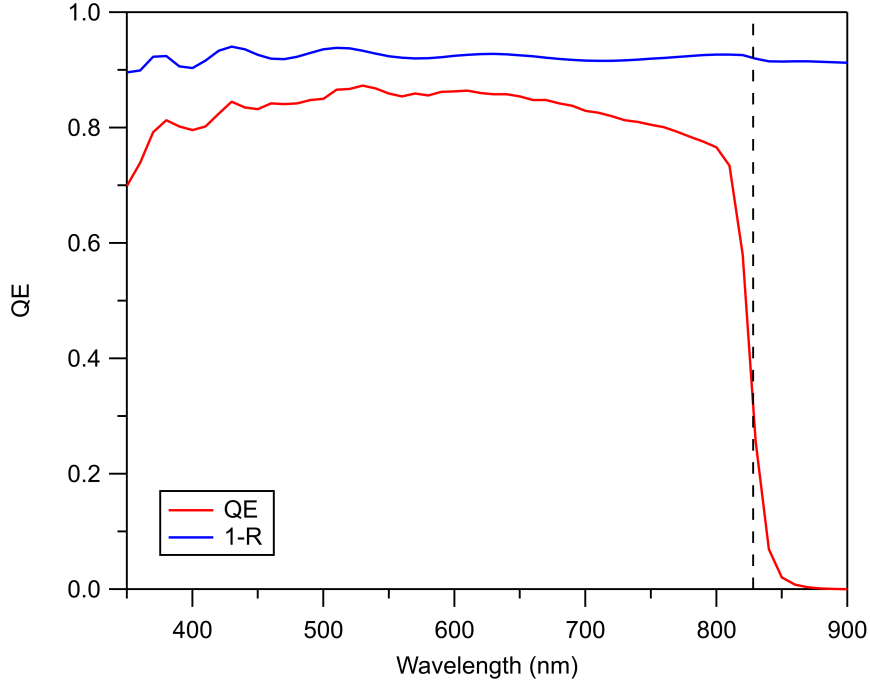


Fig. 3.2: QE and 1-R curves for a thin CdTe device with the absorption edge indicated.

The inverse relationship between absorption coefficient and depth can become especially problematic for very thin absorber layers where red light may pass right through resulting in incomplete absorption. An example of this is illustrated in Fig. 3.3 showing QE and 1-R curves for CdTe absorbers ranging 0.6  $\mu\text{m}$  to 1.2  $\mu\text{m}$  in thickness. As CdTe thickness decreases, so does the QE signal at the back of the devices. A technique for determining the particular source of losses is outlined in Section 3.4.1.

All QE data presented in this work were measured using a halogen light source passing through an Acton SpectraPro 150 monochromator followed by a SRS SR540 chopper. Optics are used to focus the monochromatic beam onto the cell. The output QE signal is amplified using a SRS SR570 amplifier and then measured by a SRS SR810 lock-in amplifier locked to the chopper's frequency. A 620 nm long-pass filter was inserted in the beam at the 650 nm point to simulate spectral conditions of AM1.5G. The QE measurement system also has the capability of applying both light and voltage bias but neither was found necessary.

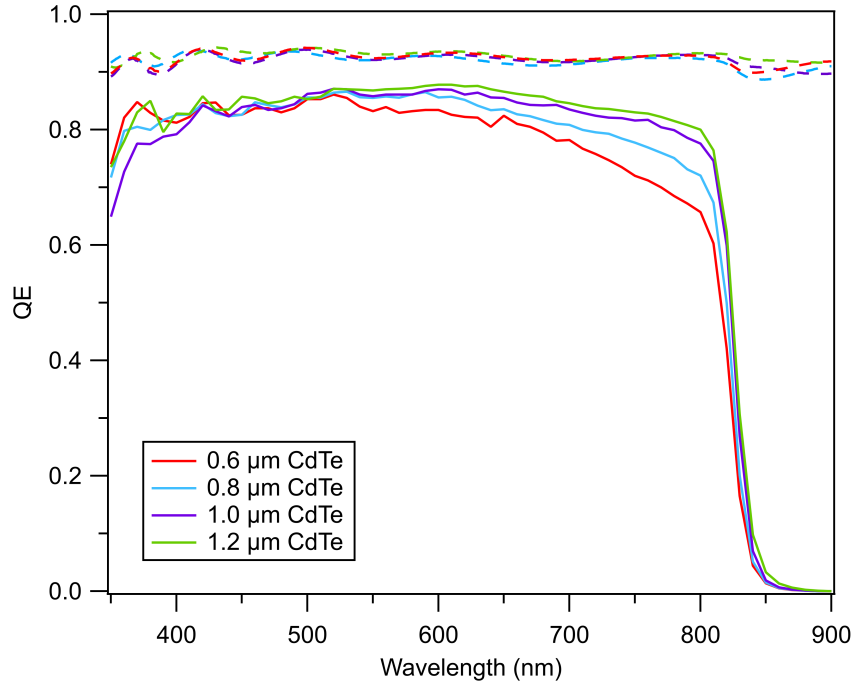


Fig. 3.3: QE and 1–R curves for CdTe devices made with absorber thicknesses ranging from 0.6  $\mu\text{m}$  to 1.2  $\mu\text{m}$ . Thinner devices suffer more losses due to incomplete absorption.

### 3.3 Electroluminescence

Electroluminescence (EL) is a characterization technique useful in quantifying solar cell uniformity. When making an EL measurement, a device is operated similar to a light-emitting diode (LED) in that current is applied to the cell which results in light emission. While operated in forward bias, electrically excited carriers recombine radiatively resulting in the emission of a photon. The cell’s photoemission is captured via a CCD camera and then processed to evaluate cell performance. Fig. 3.4 illustrates three examples of EL images of CdTe cells made at CSU; one is generally uniform while the other two are chosen to illustrate non-uniformity and defects.

All EL images were taken in a dark chamber using a Finger Lakes MicroLine ML8300 Si-CCD camera operated at  $-25^{\circ}\text{C}$  to reduce thermal noise. An injection current of 40  $\text{mA}/\text{cm}^2$  and 100 second exposure time is used for all devices. The resulting CCD image is background-subtracted, normalized to injection current and exposure time, and scaled

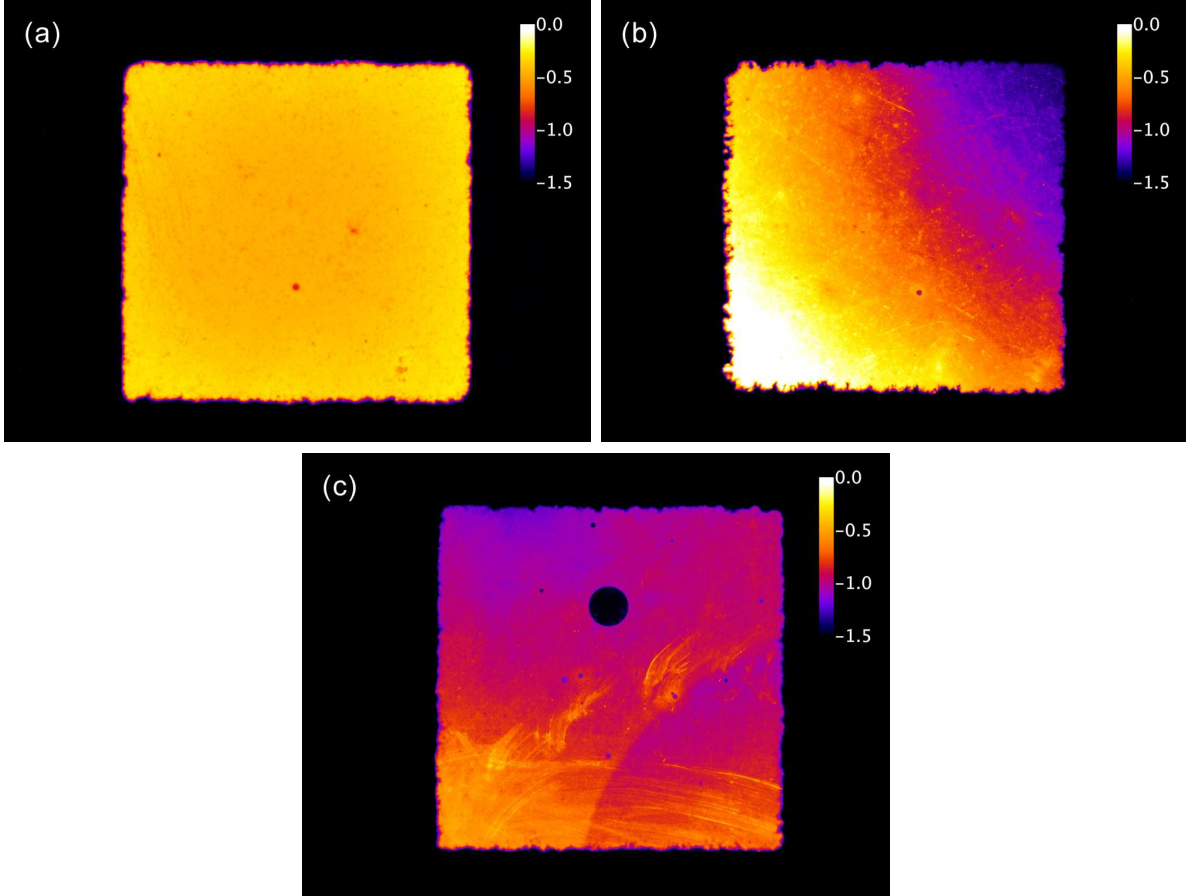


Fig. 3.4: EL images of thin CdTe devices made at CSU demonstrating: (a) uniformity, (b) non-uniformity, and (c) a large pinhole defect and handling scratches.

logarithmically using ImageJ software.

When recombination effects are minimized to just radiative recombination (ideality factor  $A = 1$ ), a solar cell realizes its maximum light-to-current conversion efficiency and produces the ideal  $V_{OC}$  predicted by the Shockley-Queisser limit. Similarly, when operated in reverse, the same device behaves as an ideal LED and achieves its maximum current-to-light conversion efficiency [25]. On the other hand, non-radiative recombination mechanisms lowers the conversion efficiency in both operating modes. In practice, CdTe solar cells are often dominated by defect-mediated recombination which largely limits  $V_{OC}$  values in solar cell mode, and photoemission in LED mode. As both  $V_{OC}$  and EL intensity losses are highly dependent on the presence of non-radiative recombination, it follows that the two quantities are closely correlated. This correlation is known as the reciprocity relationship and is given

by the equation [26]:

$$\ln(EQE_{LED}) = -\frac{q}{kT}(V_{OC}^{rad} - V_{OC}) \quad (3.7)$$

where  $V_{OC}^{rad}$  is the maximum theoretical  $V_{OC}$  of 1.20 V predicted in by the Shockley-Queisser limit in Section 2.1, and  $V_{OC}$  is the device's measured value. Similar to solar cell QE, the LED EQE ( $EQE_{LED}$ ) represents the ratio of photons emitted through electron-hole recombination to the total number of injected carriers.

EL images processed in the method described earlier will produce results proportional to  $\ln(EQE_{LED})$ , thus plotting the mean EL intensity of a cell versus it's  $V_{OC}^{rad} - V_{OC}$  value should produce a straight line with slope  $-q/kT$ . This is demonstrated in Fig. 3.5 which validates the reciprocity relationship using several CdTe and Ga-based solar cells.

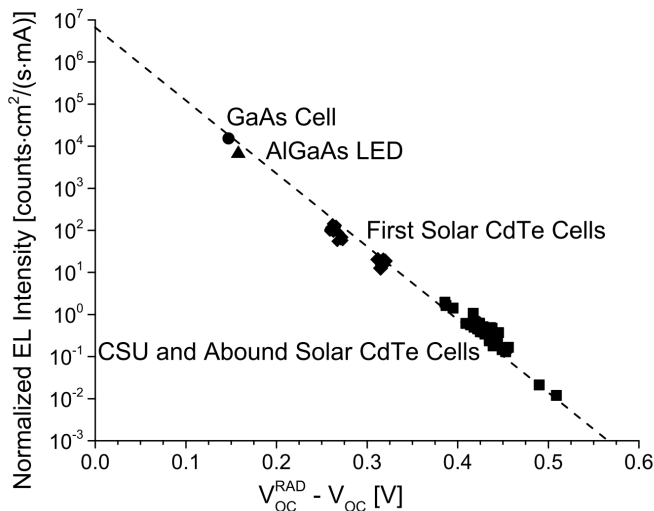


Fig. 3.5: Several solar cells illustrating the reciprocity relationship between  $V_{OC}$  and EL intensity. The fitted line had an inverse slope of -25 mV at room temperature. From Ref. [25].

## 3.4 Performance Loss Analysis

This section outlines techniques for quantifying the current and fill factor losses of CdTe solar cells.

### 3.4.1 Current Losses

Due to the superstrate nature of CdTe solar cells, a cell is a multi-layer optical stack through which light must first pass before reaching the absorber layer. These layers include the soda-lime glass, TCO and MZO window layer, and represent a series of transmission losses which occur before carrier generation. While these layers are selected to have minimal absorption, they still account for measurable current losses in CdTe devices.

In addition to the absorption of each layer, one must also consider each optical interface with its unique set of refractive indices as shown in Fig. 3.6. The cell's front structure induces a certain amount of reflection at each interface before the CdTe absorber, including: (1) air/glass, (2) glass/TCO, (3) TCO/MZO, and (4) MZO/CdTe, all of which can be combined into the front-surface reflection term,  $R_F$ . The front-surface reflection can be measured on a completed device with a spectrophotometer.

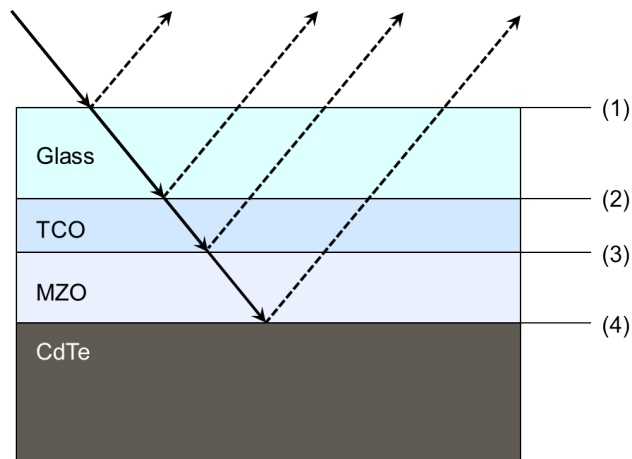


Fig. 3.6: Front-surface reflection in a MZO/CdTe solar cell.

After passing through the front layers of the device, the fraction of incident light remaining to be absorbed by the CdTe bulk becomes reduced by the product of transmission loss

coefficients [22]:

$$\begin{aligned} T_{CdTe}(\lambda) &= T_G \left(1 - R_F(\lambda)\right) \left(1 - A_{TCO}(\lambda)\right) \left(1 - A_W(\lambda)\right) \\ &= T_G T_{(1)} T_{(2)} T_{(3)} \end{aligned} \quad (3.8)$$

where  $T_G$  is the grid-shadowing factor and is equal to 1 in our gridless design.  $A_{TCO}$  is the absorption of a TCO-coated glass product like TEC10, and  $A_W$  is the absorption of the window layer.

Equation 3.8 was adapted as it was found that combining interfaces (1) through (3) in absorption measurements produced more reliable spectroscopy data by not introducing artificial interfaces with air. The adapted equation for the fraction of transmitted light incident on CdTe is:

$$\begin{aligned} T_{CdTe}(\lambda) &= T_G \left(1 - R_F(\lambda)\right) \left(1 - A_{TEC10/MZO}(\lambda)\right) \\ &= T_G T_{(1)} T_{(2,3)} \end{aligned} \quad (3.9)$$

where  $A_{TEC10/MZO}$  represents the absorption of MZO deposited on TEC10. The first transmission coefficient accounts for full device reflection using the front-facing reflection term,  $R_F$ :

$$T_{(1)}(\lambda) = \left(1 - R_F(\lambda)\right). \quad (3.10)$$

The second transmission coefficient at interfaces (2,3) is given as:

$$T_{(2,3)}(\lambda) = \left(1 - A_{TEC10/MZO}(\lambda)\right) \quad (3.11)$$

and is found by measuring absorption of MZO deposited on TEC10.

Once the transmission coefficients are found, one can start analyzing the absorption of each individual layer depicted in Fig. 3.6. Absorption measurements were made on three configurations: plain soda-lime glass, TEC10, and TEC10 with 100 nm MZO deposited. All

three absorption measurements are approximately corrected with  $1 - R_F$  by:

$$A'(\lambda) = T_{(1)} A(\lambda). \quad (3.12)$$

Lastly, a device without a back contact was fabricated; transmission on such a device represents the fraction of unabsorbed photons in a completed device. The CdTe transmission coefficient,  $T_{CdTe}$ , was calculated using Eqn. (3.8) and the transmission data was corrected using the equation:

$$T'(\lambda) = T_{CdTe} A(\lambda). \quad (3.13)$$

When plotted along with QE and  $1 - R_F$ , the  $1 - A'$  and  $1 - T'$  curves form a plot that is useful in visualizing sources of current losses. Two such plots are shown in Fig. 3.7. The superposition of light and dark regions in blue represents all carriers generated, while the remaining regions are considered losses external to the CdTe absorber. Together, all regions are additive and collectively account for 100% of incident photons.

With the exception of the light blue, the area of each region represents the current lost from the cell's maximum theoretical current. By integrating each area along with the AM1.5G spectrum, the associated current losses can be calculated by:

$$J_{f(\lambda)} = \int_0^{\lambda_G} f(\lambda) \frac{\lambda P(\lambda)}{hc} d\lambda \quad (3.14)$$

where  $f(\lambda)$  is an optical measurement such as QE, reflection, transmission or absorption, and  $P(\lambda)$  is the irradiation of the AM1.5G spectrum. When all current losses are calculated, they are summed together with the cell current to calculate the cell's maximum current density. Table 3.1 shows the calculated losses and maximum current for the 0.6 and 1.0  $\mu\text{m}$  CdTe devices.

Optical losses due to reflection and window layer absorption are assumed to be constant for all devices made on nominally-identical superstrates of 100 nm MZO on TEC10. As

Table 3.1: Maximum theoretical current and current losses for the devices shown in Fig. 3.7

(mA/cm <sup>2</sup> )	0.6 $\mu$ m CdTe	1.0 $\mu$ m CdTe
Cell current	21.9	24.0
Reflection losses	2.1	2.1
Glass absorption	1.0	1.0
TCO absorption	1.1	1.1
MZO absorption	0.1	0.1
Unabsorbed photons	1.6	0.6
Recombination losses	1.2	0.1
Maximum current	28.9	28.9

demonstrated in Fig. 3.7 and Table 3.1, the 0.6  $\mu$ m device suffers greater current loss from incomplete absorption due to the transparent nature of CdTe deposited in such thin layers. Additionally, the thinner device also has more recombination loss throughout most of the visible spectrum indicating a smaller diffusion length. Time-resolved photoluminescence (TRPL) results in Fig. 3.8 illustrate that thinner CdTe layers have shorter minority carrier lifetimes. In particular, minority carrier lifetimes halve when thinning the CdTe layer from 1.0  $\mu$ m down to 0.6  $\mu$ m, leading to the increase in recombination observed.

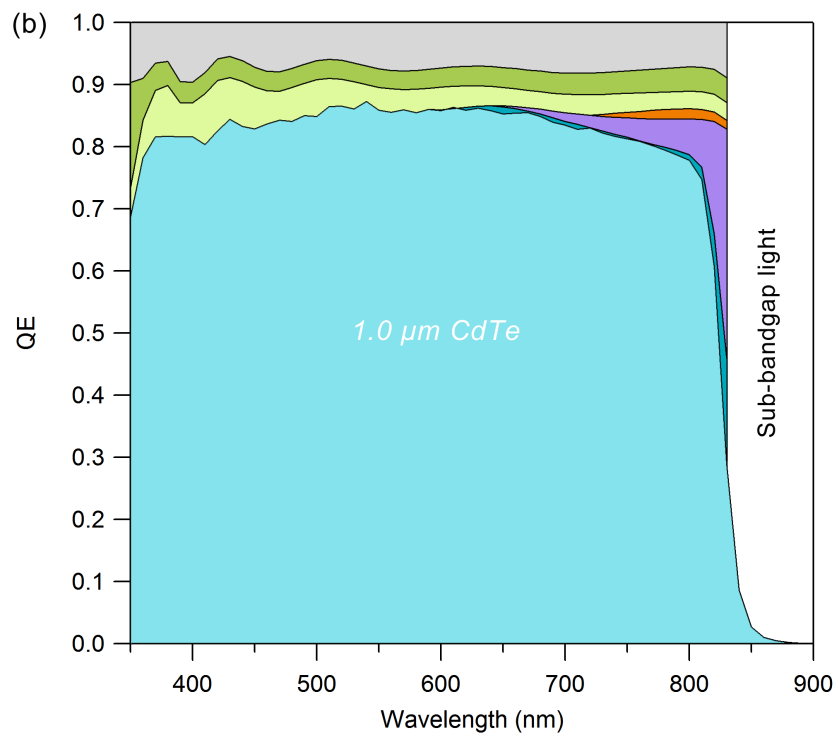
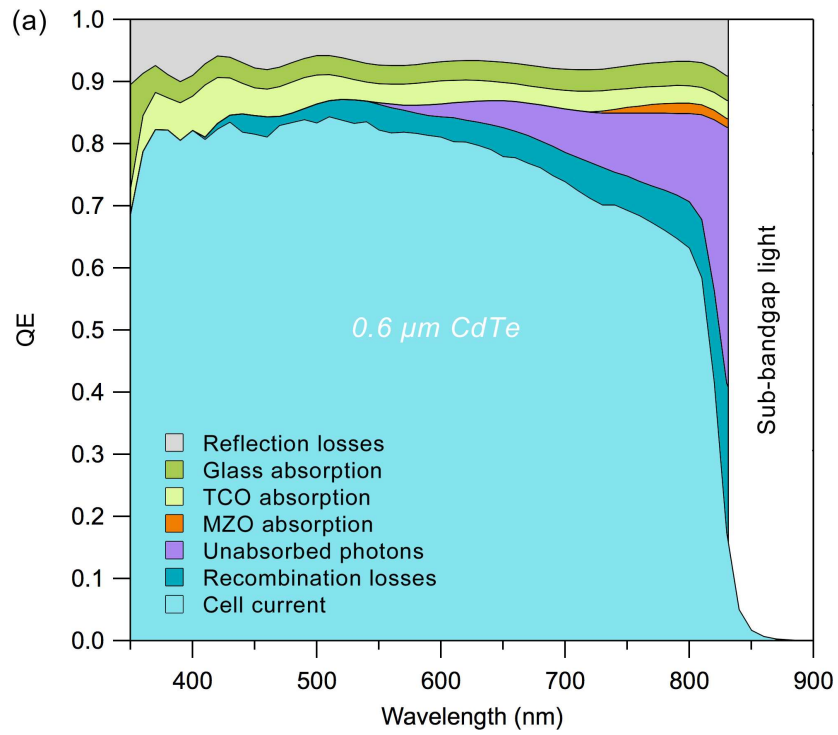


Fig. 3.7: Current losses of: (a) 0.6  $\mu\text{m}$ , and (b) 1.0  $\mu\text{m}$  CdTe devices.

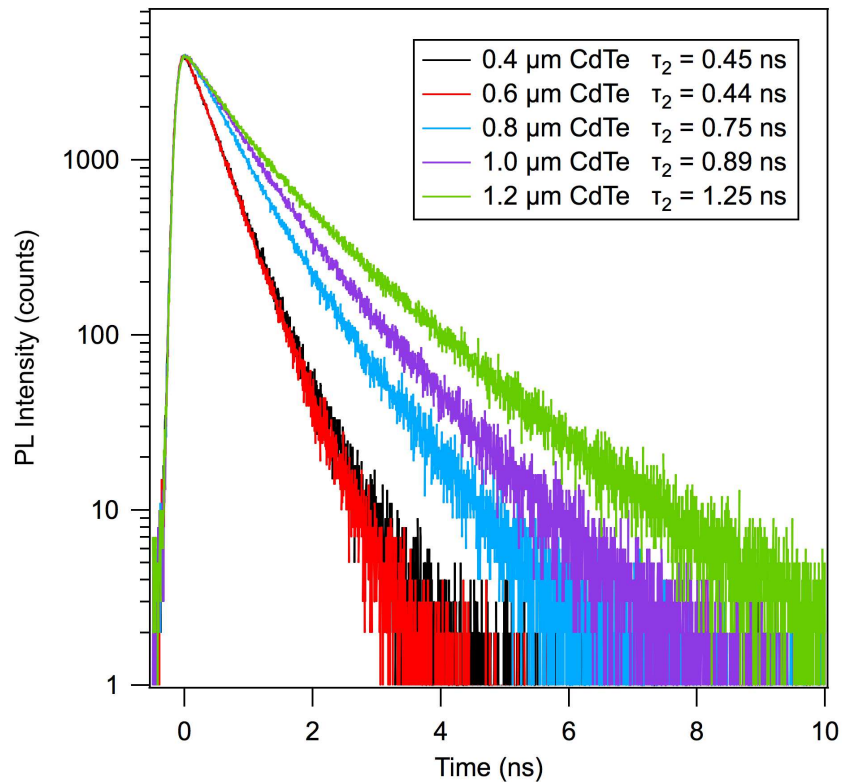


Fig. 3.8: TRPL results for devices with CdTe absorbers ranging 0.4  $\mu\text{m}$  to 1.2  $\mu\text{m}$  thick, measured from the glass side. A thinner CdTe layer generally leads to shorter minority carrier lifetimes. Credit: Darius Kuciauskas.

### 3.4.2 Fill Factor Losses

A solar cell's measured fill factor can be considered a product of its ideal fill factor,  $FF_0$ , and a loss coefficient,  $\alpha$ , such that:

$$FF = \alpha FF_0 \quad (3.15)$$

where  $0 \leq \alpha \leq 1$ . Thus, fill factor losses can be characterized by a ratio such that:

$$\alpha = \frac{FF}{FF_0} \quad (3.16)$$

The theoretical limits of CdTe performance based on AM1.5G conditions at 25°C were calculated in Section 2.1 and corresponded to  $V_{OC} = 1.20$  V and  $J_{SC} = 29.3$  mA/cm<sup>2</sup>, which results in a maximum theoretical fill factor of  $FF_0 = 89.8\%$ .

The loss coefficient,  $\alpha$ , can be separated into factors to account for individual deviations due to non-ideal diode behavior as well as parasitic effects:

$$\alpha = \frac{FF}{FF_0} = \delta_{diode} \delta_{series} \delta_{shunt} \delta_{other} \quad (3.17)$$

$$\frac{FF}{FF_0} = \left[ \frac{FF_{A',V'_{OC}}}{FF_{A=1,V_{OC}=1.20 \text{ V}}} \right] \delta_{series} \delta_{shunt} \delta_{other} \quad (3.18)$$

where  $\delta_{diode}$  is the bracketed term

$$\delta_{diode} = \left[ \frac{FF_{A',V'_{OC}}}{FF_{A=1,V_{OC}=1.20 \text{ V}}} \right] \quad (3.19)$$

and represents the ratio of predicted-to-ideal fill factor based on measured  $A'$  and  $V'_{OC}$  values. The numerator and denominator of Eqn. 3.19 are calculated using the thermal-voltage normalized  $\nu_{OC} = qV_{OC}/AkT$  and can be predicted analytically for  $\nu_{OC} > 10$  to four

significant digits using the equation [8]

$$FF_{A,V_{OC}} = \frac{V_{OC} - \ln(V_{OC} + 0.72)}{V_{OC} + 1}. \quad (3.20)$$

$\delta_{series}$  and  $\delta_{shunt}$  represent losses due to series resistance and shunt conductance respectively, while finally,  $\delta_{other}$  represents voltage-dependent photocurrent and all other losses not accounted for directly. To avoid coupling between terms, this analysis is best applied only to devices with high fill factors ( $>70\%$ ).

Losses due to non-ideal  $V_{OC}$  and  $A$  values can be further separated by expanding the term in square brackets

$$\frac{FF}{FF_0} = \left[ \frac{FF_{A',V'_{OC}}}{FF_{A=1,V_{OC}=1.20 \text{ V}}} \right] \delta_{series} \delta_{shunt} \delta_{other} \quad (3.21)$$

$$\frac{FF}{FF_0} = \left[ \frac{FF_{A=1,V'_{OC}}}{FF_{A=1,V_{OC}=1.20 \text{ V}}} \frac{FF_{A',V'_{OC}}}{FF_{A=1,V'_{OC}}} \right] \delta_{series} \delta_{shunt} \delta_{other} \quad (3.22)$$

The first term in brackets represents losses due to a reduction in  $V_{OC}$ , while the second term represents losses due to a higher ideality factor. Together, both of these mechanisms represent losses due to non-idealities within the diode itself.

After the series resistance and shunt conductance,  $R$  and  $G$ , are found from a J-V analysis like the one outlined in Section 3.1, then parasitic losses can be characterized through a technique developed by Ref. [8] to determine  $\delta_{series}$  and  $\delta_{shunt}$ . Defining the characteristic resistance of a cell to be

$$R_{CH} = \frac{V_{OC}}{J_{SC}} \quad (3.23)$$

then the series resistance,  $R$ , can be normalized to this value by

$$r = \frac{R}{R_{CH}} \quad (3.24)$$

The relative loss of fill factor due to series resistance can then be approximated to two

significant figures for  $r < 0.4$  by the equation

$$\delta_{series} \approx 1 - r. \quad (3.25)$$

Similarly, a normalized shunt conductance term is defined as

$$g = \frac{1}{GR_{CH}} \quad (3.26)$$

and the relative loss of fill factor due to shunt conductance is approximated to three significant digits for  $\nu_{OC} > 10$  and  $g > 2.5$ :

$$\delta_{shunt} \approx 1 - \frac{\nu_{OC} + 0.7 FF_0}{\nu_{OC} g}. \quad (3.27)$$

The results of fill factor loss analysis are outlined in Table 3.2 for two well performing devices of different CdTe thicknesses made at CSU. One with a thin CdTe absorber of 1.3  $\mu\text{m}$  had an efficiency of 14.0%, while the other with a thicker 3.0  $\mu\text{m}$  CdTe layer had an efficiency of 18.3%. J-V parameters for the same devices are also provided in Table 3.3 for reference.

Table 3.2: Relative fill factor losses calculated for two CdTe devices with different absorber thicknesses.

Loss Mechanism	Relative Loss	
	1.3 $\mu\text{m}$ CdTe	3.0 $\mu\text{m}$ CdTe
$FF_{A=1.0, V'_{OC}} / FF_{A=1.0, V_{OC}=1.20 V}$	0.962	0.967
$FF_{A', V'_{OC}} / FF_{A=1.0, V'_{OC}}$	0.906	0.967
$\delta_{series}$	0.974	0.969
$\delta_{shunt}$	0.967	0.992
$\delta_{other}$	0.986	0.981
Measured $FF$	0.727	0.792
$FF_0$	0.898	0.898

The relative losses from 1.000 can be normalized to the difference between measured

Table 3.3: J-V parameters for two CdTe devices with different absorber thicknesses.

	1.3 $\mu\text{m}$ CdTe	3.0 $\mu\text{m}$ CdTe
$J_{SC}$ (mA/cm <sup>2</sup> )	23.4	26.8
$V_{OC}$ (V)	0.824	0.863
$FF$ (%)	72.7	79.2
$\eta$ (%)	14.0	18.3
$A$	1.9	1.3
$R$ ( $\Omega\text{-cm}^2$ )	0.9	1.0
$G$ (mS/cm <sup>2</sup> )	1.0	0.3

and ideal fill factor values to produce a visual representation of absolute losses. Fig. 3.9 compares the same two cells, instead demonstrating absolute fill factor losses and how each device is most adversely affected. The thinner device suffers considerably more fill factor losses in general. Overall, diode quality is the largest difference between the two accounting for an additional 5% (absolute) fill factor loss for the thinner device. Electrical shunting accounts for the second largest difference, represented by an additional 2% fill factor loss for the thinner device. All other fill factor losses were generally comparable between both the thinner and thicker devices.

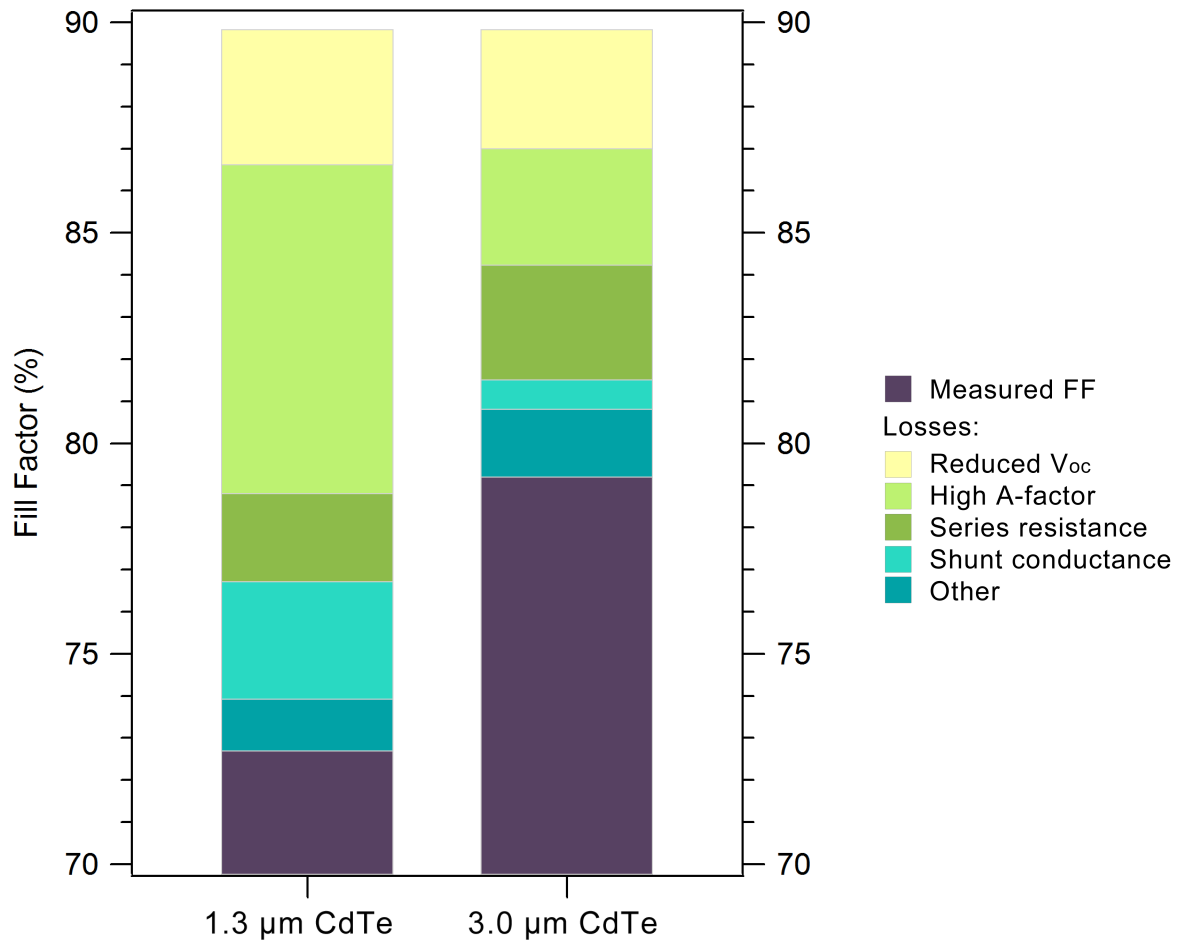


Fig. 3.9: Absolute fill factor losses for two CdTe cells made at CSU with different absorber thicknesses. Measured fill factor is represented in purple while all other regions above are considered losses from CdTe's ideal fill factor of 89.8% predicted by the Shockley-Queisser limit at standard testing conditions.

# Chapter 4

## PROCESSING OPTIMIZATION

As was described in Section 2.2,  $\text{CdCl}_2$  passivation and Cu-doping are post-deposition treatments which are key to fabricating high efficiency CdTe solar cells. First exposing the CdTe absorber to  $\text{CdCl}_2$  encourages the passivation of dangling bonds at the grain boundaries while also aiding in recrystallization and grain coalescence [16]. Following the chlorine passivation, a CuCl exposure to the back of the CdTe absorber facilitates the formation of a CuTe alloy which has been found to be helpful in forming ohmic contact with a metal.

Both post-deposition treatments involve exposing the CdTe surface to a high-temperature material followed by an annealing process. The ideal dosing and anneal times are highly dependent on absorber thickness, necessitating that these processes be optimized for the thin CdTe cell described in Section 2.3.

This chapter outlines the results of thin CdTe processing experiments conducted at CSU. Experiments of dose and anneal sweeps of both  $\text{CdCl}_2$  passivation and Cu-doping treatments were performed on CdTe cells with  $1.0\ \mu\text{m}$  absorbers. All  $\text{CdCl}_2$  and CuCl exposure was performed via close-space sublimation using the single-vacuum chamber system described in Ref. [20]. Dose was defined by the length of time the CdTe surface was exposed to the sublimating  $\text{CdCl}_2$  or CuCl material. Sweep ranges were selected to represent under-treated devices based on system-optimized work for  $2.2\ \mu\text{m}$  to  $2.5\ \mu\text{m}$  CdTe absorbers. Lastly, temperatures used were selected based on well-established standards for optimal sublimation and condensation of various materials onto CdTe films.

## 4.1 CdCl<sub>2</sub> Passivation

### 4.1.1 CdCl<sub>2</sub> Dose Sweep

In order to determine the optimal passivation treatment for a thin CdTe absorber, a sweep of CdCl<sub>2</sub> dose was performed. Following the CdTe deposition and without leaving vacuum, CdCl<sub>2</sub> was applied in varying doses followed by a constant annealing process at 400°C for 180 seconds. The dose times were 38, 58, 78, 98, 118, 138, and 158 seconds, and were selected to represent under-passivated devices based on a 180 second dose time previously optimized for thicker (>2.2 μm) absorbers.

The J-V curves for the best performing devices at each CdCl<sub>2</sub> dose are shown in Fig. 4.1 and demonstrate that devices become generally well behaved after 58 second CdCl<sub>2</sub> dose. This indicates that a minimum dose is required before the CdCl<sub>2</sub> treatment is activated.

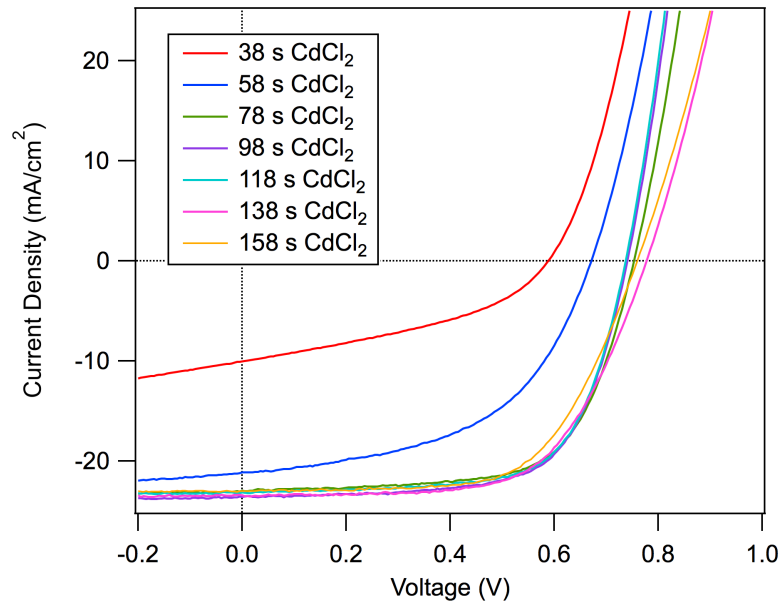


Fig. 4.1: J-V curves for best performing 1.0-μm devices at each CdCl<sub>2</sub> dose time. Performance significantly improves after 58 seconds CdCl<sub>2</sub> dose.

The results of basic J-V characterization versus CdCl<sub>2</sub> dose are shown in Fig. 4.2 for all devices fabricated. Following minimum passivation,  $V_{OC}$  and  $J_{SC}$  remain relatively flat over a wide range of doses. On the other hand, fill factor peaks before dropping off slightly. As

a result, the best conversion efficiencies occur over the range of 118 to 138 seconds  $\text{CdCl}_2$  dose.

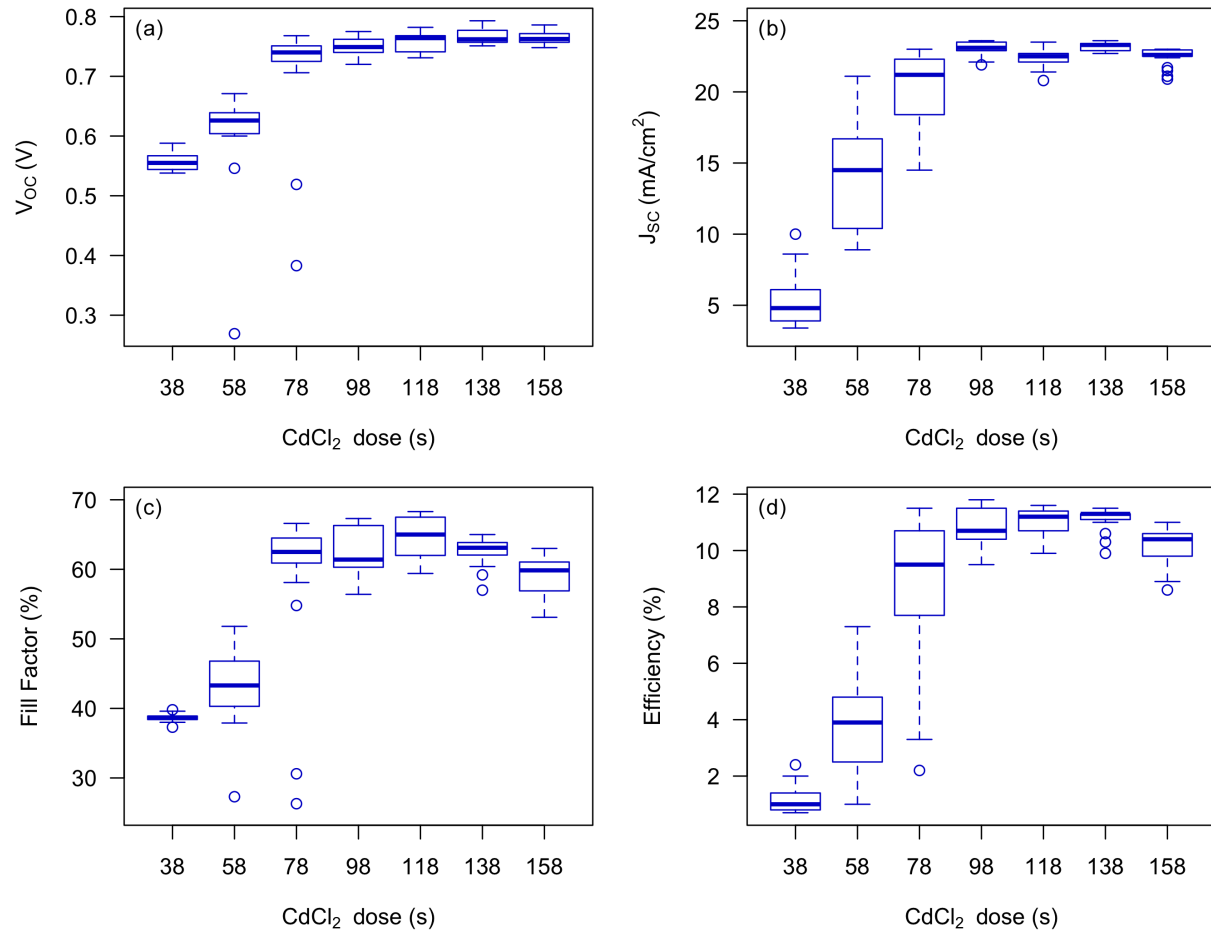


Fig. 4.2: J-V metrics as a function of  $\text{CdCl}_2$  dose time for  $1.0\text{-}\mu\text{m}$  CdTe devices. ( $n = 15 - 25$  devices, some extreme outliers were removed)

The results suggest that optimal  $\text{CdCl}_2$  dose time is fairly flexible producing comparable efficiencies over a 20 second range of  $\text{CdCl}_2$  doses. Similar  $\text{CdCl}_2$  dose sweeps were performed for thin CdTe absorbers of different thickness ranging  $0.6\text{ }\mu\text{m}$  to  $1.2\text{ }\mu\text{m}$  in  $0.2\text{ }\mu\text{m}$  increments. The results of top performing devices at each thickness are shown in Fig. 4.3 and demonstrate that optimal  $\text{CdCl}_2$  dose is also fairly flexible with absorber thickness for the given range.

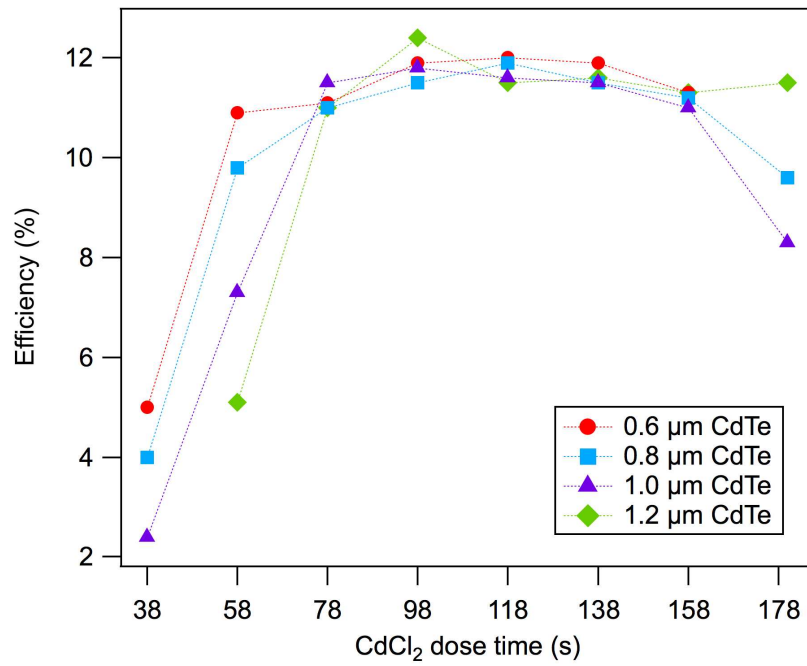


Fig. 4.3: Conversion efficiency as a function of CdCl<sub>2</sub> dose time for CdTe devices with absorber thicknesses ranging 0.6 μm to 1.2 μm.

### 4.1.2 CdCl<sub>2</sub> Anneal Sweep

The results of the previous section used a 180-second CdCl<sub>2</sub> anneal time based the system standard for thicker absorbers. As this doesn't necessarily represent an optimal annealing process for thinner CdTe absorbers, a sweep of CdCl<sub>2</sub> anneal was performed. Devices were fabricated with 1.0- $\mu\text{m}$  CdTe treated by 125 seconds of CdCl<sub>2</sub>. While still in vacuum, the CdCl<sub>2</sub> anneal time was swept from 90 to 300 seconds in 30 second intervals at a constant 400°C. After rinsing off excess CdCl<sub>2</sub>, devices were also Cu-doped to improve performance using the ideal deposition parameters that will be discussed later in Section 4.2.

The results of J-V characterization of best devices from each anneal time are shown in Table 4.1 and illustrate that they are well-behaved regardless of anneal time. There is a slight decrease in  $V_{OC}$  of approximately 20 mV with longer anneal times, while  $J_{SC}$  and fill factor are stable. Due to the slight decrease in  $V_{OC}$ , conversion efficiency also decreases slightly with longer CdCl<sub>2</sub> anneal times.

Table 4.1: J-V metrics of best performing devices as a function of CdCl<sub>2</sub> anneal time.

CdCl <sub>2</sub> anneal (s)	$J_{SC}$ (mA/cm <sup>2</sup> )	$V_{OC}$ (V)	$FF$ (%)	$\eta$ (%)
90	23.1	0.826	70.9	13.5
120	23.2	0.817	71.2	13.5
150	23.4	0.812	70.0	13.3
180	23.3	0.815	69.7	13.3
210	23.4	0.817	67.5	12.9
240	23.3	0.808	68.9	13.0
270	23.3	0.807	70.8	13.3
300	23.1	0.805	69.4	12.9

Further J-V characterization for all devices fabricated is shown in Fig. 4.4 and illustrates similar trends as the ones demonstrated in Table 4.1. The median  $V_{OC}$  decreases slightly with longer anneal times while  $J_{SC}$  and fill factor are relatively stable. From Fig. 4.4(d), we find the best performance occurs at 120 seconds CdCl<sub>2</sub> anneal time, both in highest median value and the smallest range of interquartile data

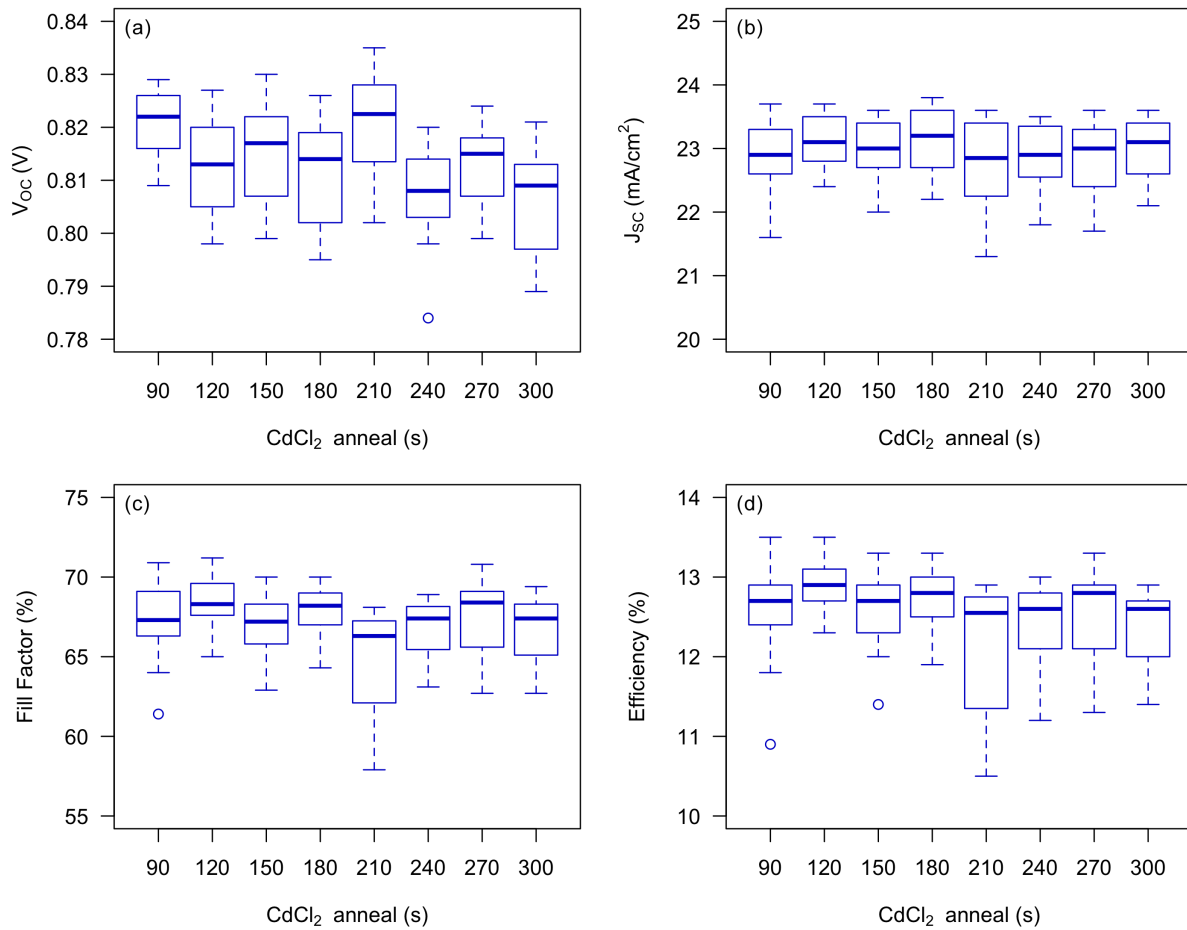


Fig. 4.4: J-V metrics as a function of CdCl<sub>2</sub> anneal time for 1.0-μm CdTe devices. ( $n = 23 - 25$  devices, some extreme outliers were removed)

## 4.2 Cu-doping

### 4.2.1 CuCl Dose Sweep

To optimize the Cu-doping process for thin CdTe absorbers, a sweep of CuCl dose time was performed. CdTe devices with a 1.0- $\mu\text{m}$  absorber were fabricated and passivated with 120-seconds of  $\text{CdCl}_2$  treatment followed by a 180-second anneal at 400°C. Once rinsed of excess  $\text{CdCl}_2$  and back in the deposition system, CuCl was then sublimated onto the CdTe surface followed by a 220-second anneal at 200°C. Based on a system-optimized CuCl dose of 30 seconds for thicker CdTe absorbers, the CuCl dosing was varied from 0 to 10 seconds in intervals of 2 seconds. Excess CuCl material was also rinsed off afterwards using deionized water.

The results of J-V characterization as a function of CuCl dose time are shown in Fig. 4.5. Fig. 4.5(a) demonstrates Cu-doping improves  $V_{OC}$  both in value and reproducibility of results. On the other hand, Fig. 4.5(b) and (c) illustrate a trade-off between minimally increasing  $J_{SC}$  and rapidly decreasing fill factor. Compare these results to Fig. 4.6 for simulated CdTe devices which demonstrates the relationship between back surface carrier density and carrier lifetime on J-V metrics. From Fig. 4.6(a) and (b), we see improvements to  $J_{SC}$  and  $V_{OC}$  are largely dependent on back surface carrier density. Meanwhile, Fig. 4.6(c) illustrates that changes in fill factor are more dependent on carrier lifetimes.

These results suggests that the devices in Fig. 4.5 are experiencing increasing back surface carrier density and decreasing bulk carrier lifetime as CuCl dose increases. As carrier lifetimes have more direct impact on cell performance, it follows that the highest efficiency devices were produced at 2 seconds CuCl dose. Such a short dose time is consistent with literature which suggests that one should err on the side of under-doping rather than over-doping, the latter of which leads to severe long-term stability issues [19].

In addition to higher photoconversion efficiency, another benefit of Cu-doping is improved uniformity across a cell. This is illustrated in Fig. 4.7 which shows EL images of six cells

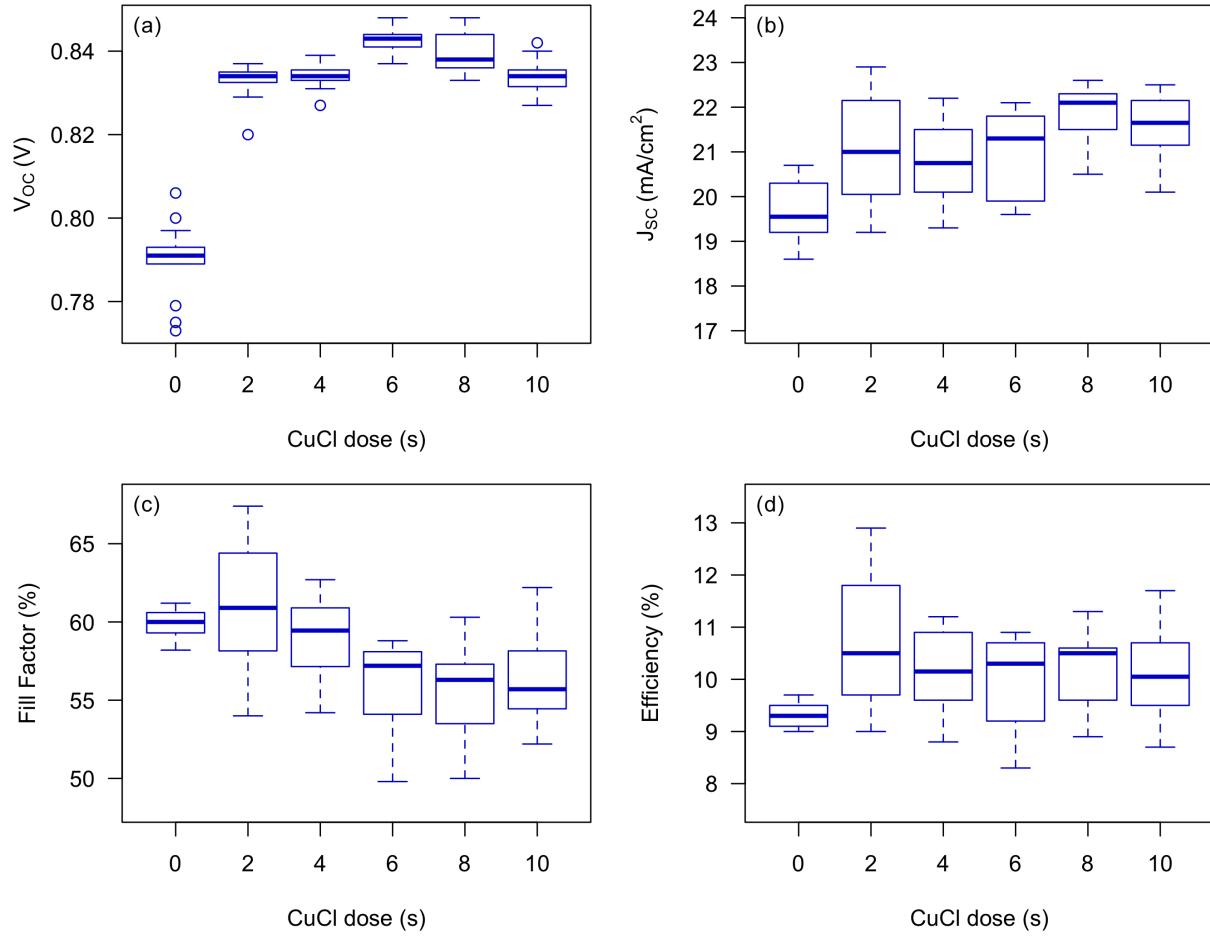


Fig. 4.5: J-V metrics as a function of CuCl dose time for 1.0- $\mu\text{m}$  CdTe devices. ( $n = 13 - 19$  devices, some extreme outliers were removed)

with CuCl doses ranging from 0 to 10 seconds. The device without any Cu has a gradient of poor performance across the width of the cell. Cells that are Cu-doped become significantly improved in both performance and uniformity. Additionally, a small decrease in intensity can be seen as CuCl dose increases from 2 to 10 seconds indicating the detrimental effects of over-doping.

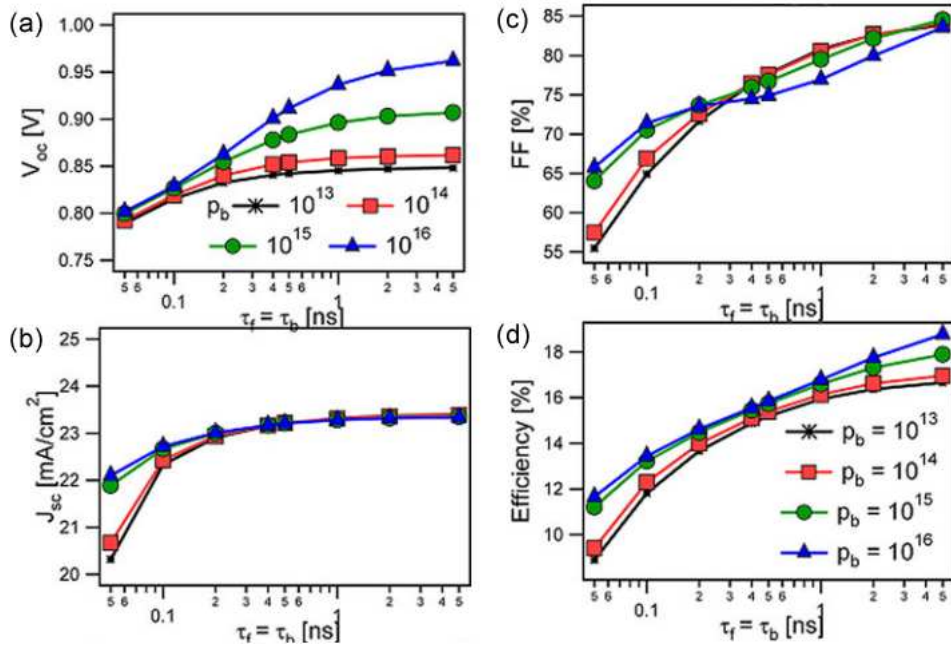


Fig. 4.6: The effects of carrier lifetime and back surface doping on 4.0- $\mu\text{m}$  CdTe devices modeled with non-uniform carrier lifetimes throughout the absorber. The last micrometer of CdTe near the back is doped with the  $p_b$  values indicated, while the remaining absorber has carrier density  $10^{13} \text{ cm}^{-3}$ . These carrier density values are a reasonable estimate of those produced in thicker devices at CSU. From Ref. [27].

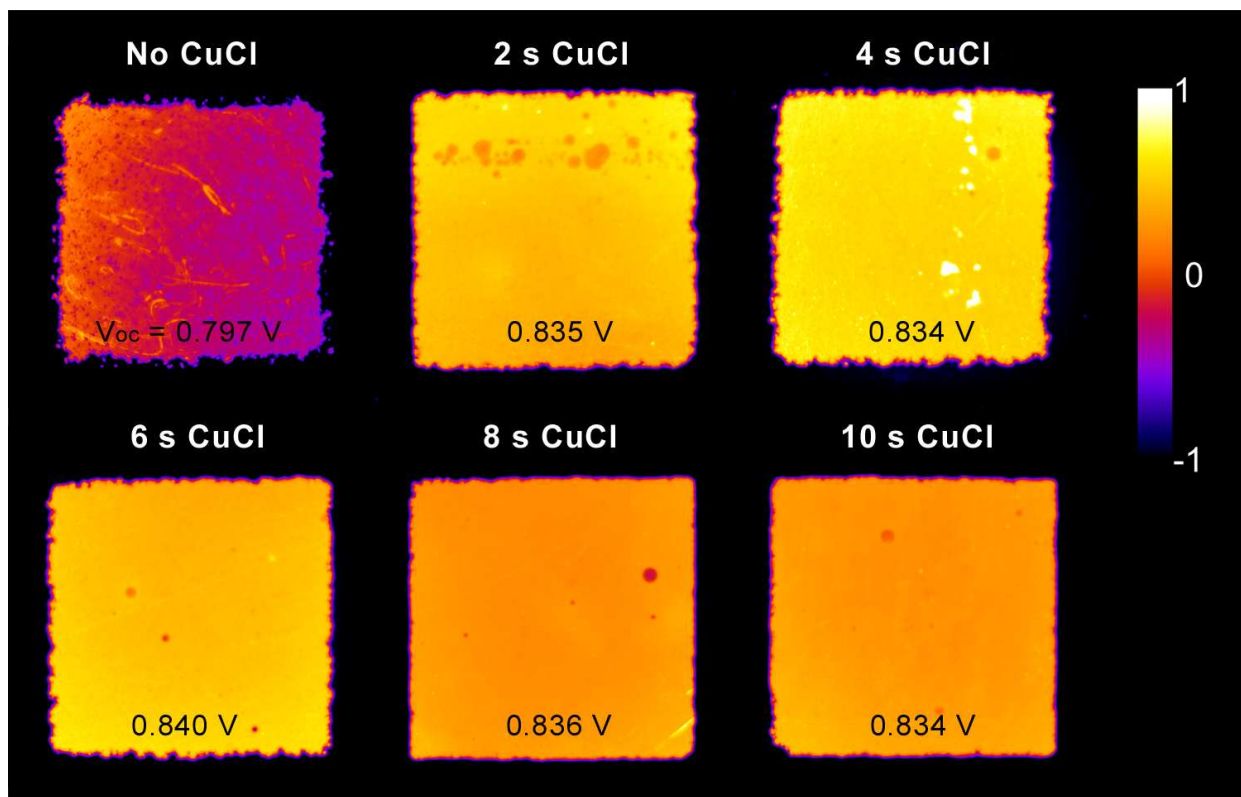


Fig. 4.7: EL images of devices exposed to 0-10 seconds CuCl treatment in 2 second intervals. Device uniformity significantly improves with the addition of copper, while overall performance decreases slightly with longer CuCl doses.

## 4.2.2 CuCl Anneal Sweep

The CuCl anneal time used in Section 4.2.1 was based on the system-optimized anneal for thicker CdTe absorbers ( $>2.2\ \mu\text{m}$ ). To find an optimal CuCl anneal time for thin  $1.0\text{-}\mu\text{m}$  absorbers, CuCl doses of 2, 6 and 10 seconds were selected based on the results of Section 4.2.1. For each CuCl dose, anneal times of 35, 45, 55, 110 and 220 seconds at  $400^\circ\text{C}$  were used. It was assumed that there is a lower limit to good performance and anneal times significantly shorter than 35 s will also produce poor devices. The results of J-V characterization by CuCl anneal time are shown in Fig. 4.8.

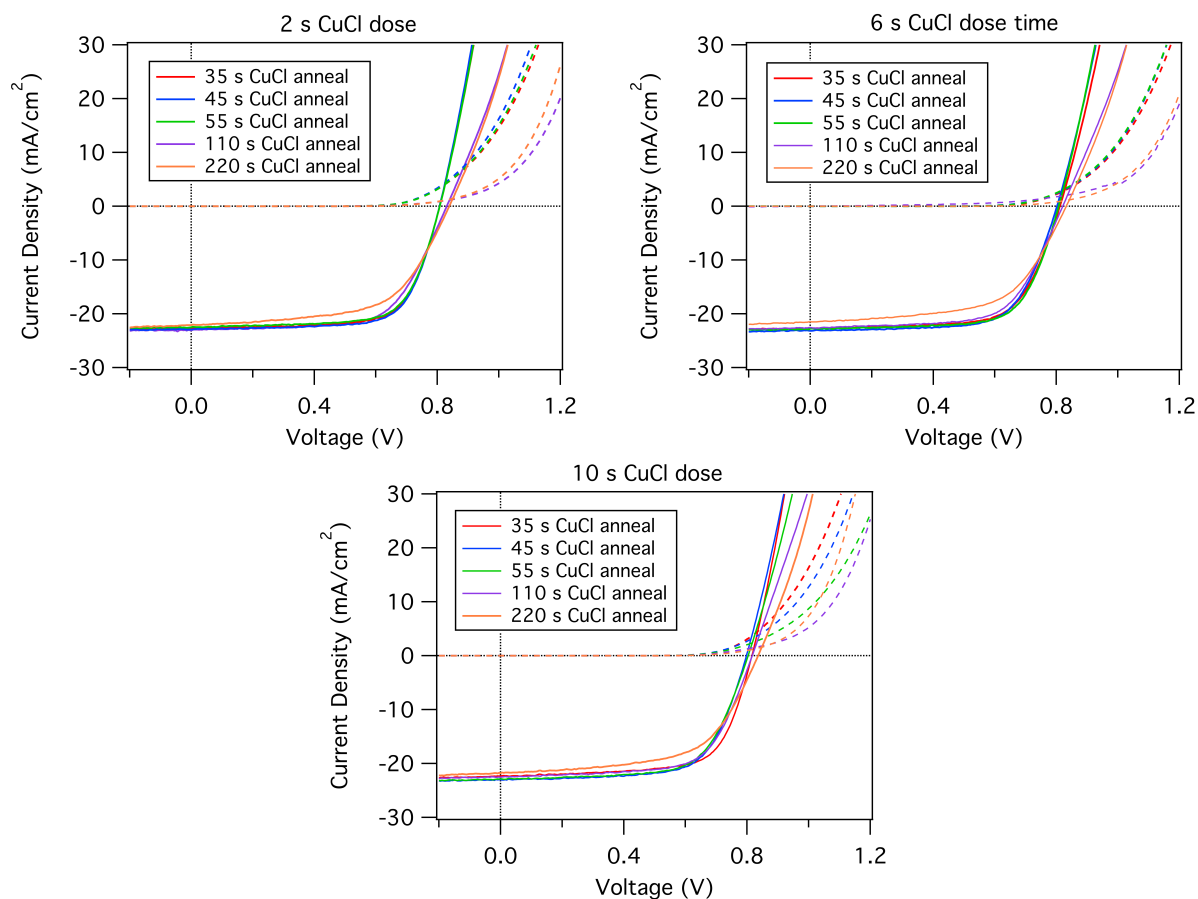


Fig. 4.8: J-V curves of  $1.0\text{-}\mu\text{m}$  CdTe devices with 2, 6 and 10 seconds of CuCl treatment followed by 35-220 seconds of annealing. J-V crossover appears to worsen with longer CuCl doses and anneal times.

Fig. 4.8 illustrates that devices were generally well-behaved. Longer CuCl anneal times appeared to result in increased crossover between light and dark curves, an effect which is

also enhanced by longer CuCl doses as well. This is consistent with an increasing number of donor-type defects [28].

J-V metrics as a function of CuCl anneal time are shown in Fig 4.9 for 2, 6 and 10 seconds CuCl dose, in blue, red, and green respectively. The results illustrate several similar trends across all three CuCl dose times: a general increase in  $V_{OC}$ , while  $J_{SC}$ , fill factor and conversion efficiency decrease at longer anneal times. Longer CuCl dose times also appeared to produce overall slightly poorer performance. As a result, the overall best conversion efficiencies occurred between 35 to 55 seconds anneal for 2 seconds of CuCl deposition.

Since fill factors experienced the greatest losses at higher CuCl anneal times, a fill factor analysis was performed similar the one outlined in Section 3.4.2. The results as a function of CuCl dose are shown in Fig. 4.10. The purple area represents fill factor measured, while the regions above represent losses from the ideal CdTe fill factor of 89.8% predicted by the Shockley-Queisser limit in Section 2.1.

Lower CuCl anneal times corresponded to higher measured fill factors with minimized losses. Additionally, series and shunt resistance together account for the largest source of fill factor loss at longer CuCl anneal times. This may be indicative of Cu atoms diffusing via grain boundaries towards the  $p-n$  junction as is known to happen in Cu-doped CdTe devices when under high temperature stress [29]. As Cu contamination at the  $p-n$  junction would decrease the diode effectiveness, it follows that the ideality factor would increase as well for longer CuCl anneal times.

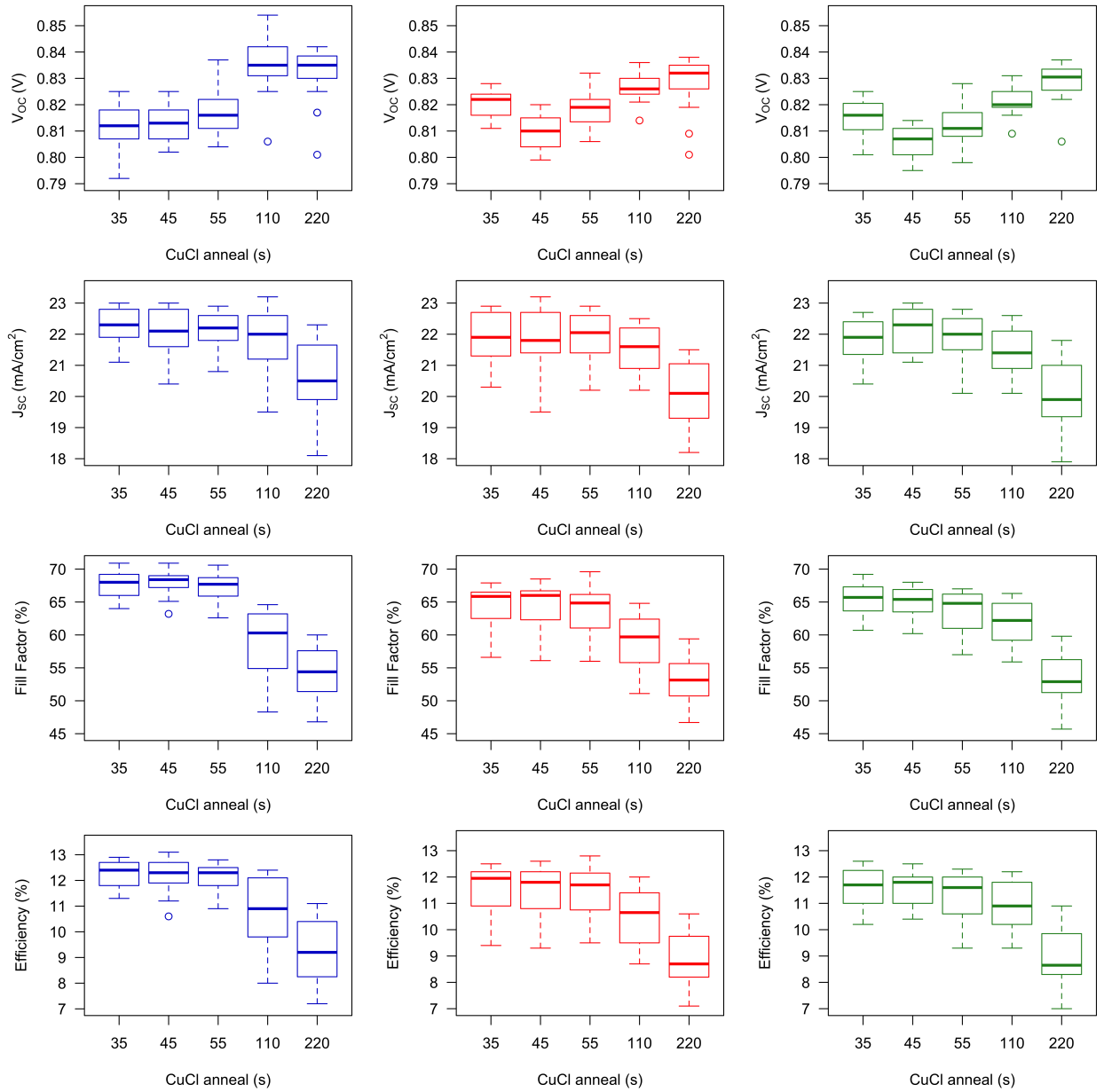


Fig. 4.9: J-V metrics as a function of CuCl dose and anneal time for 1.0- $\mu\text{m}$  CdTe devices. 2, 6 and 10 second CuCl doses are shown in blue, red and green respectively. ( $n = 21 - 25$  devices, some extreme outliers were removed)

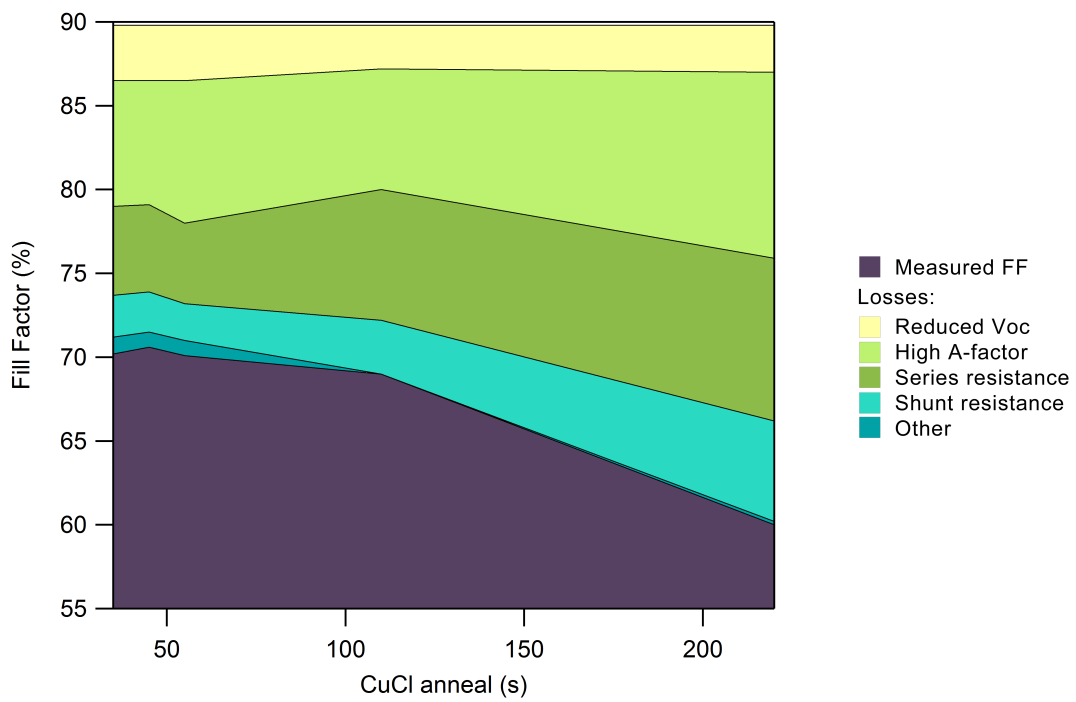


Fig. 4.10: Fill factor losses as a function of CuCl anneal time. Longer CuCl anneal times lead to lower fill factors and greater parasitic losses.

# Chapter 5

## EFFECTS OF CADMIUM TELLURIDE GROWTH TEMPERATURE

Nucleation temperatures are known to affect both the physical and stoichiometric properties of CdTe films. Higher deposition temperatures increase grain size and lower parasitic effects leading to improved  $V_{OC}$  [30]. However, high growth temperatures are also associated with Te-richness and lower carrier lifetimes [31].

This section focuses on the results of CdTe growth temperature experiments conducted at CSU. Growth of 1.0- $\mu\text{m}$  CdTe films were attempted at two temperatures of approximately 460°C (“standard temperature”), and 610°C (“high temperature”). The temperatures selected were based on previous system-optimized experiments, where growth temperature is defined by the temperature of the glass plate as it enters the CdTe deposition chamber.

### 5.1 Voltage-dependent Collection

Fig. 5.1 shows the J-V curves for devices of similar absorber thicknesses grown at standard and high temperatures. High temperature devices appear to consistently achieve higher  $V_{OC}$  values, however, also suffer from significant fill factor and  $J_{SC}$  losses as shown in Table 5.1. These losses are largely due to voltage-dependent photocurrent which appears related to CdTe growth temperature.

Table 5.1: Average J-V metrics for the devices depicted in Fig. 5.1.

	ST CdTe	HT CdTe
$J_{SC}$ (mA/cm <sup>2</sup> )	23.0	19.9
$V_{OC}$ (V)	0.751	0.799
FF (%)	68.5	55.3
$\eta$ (%)	11.8	8.8

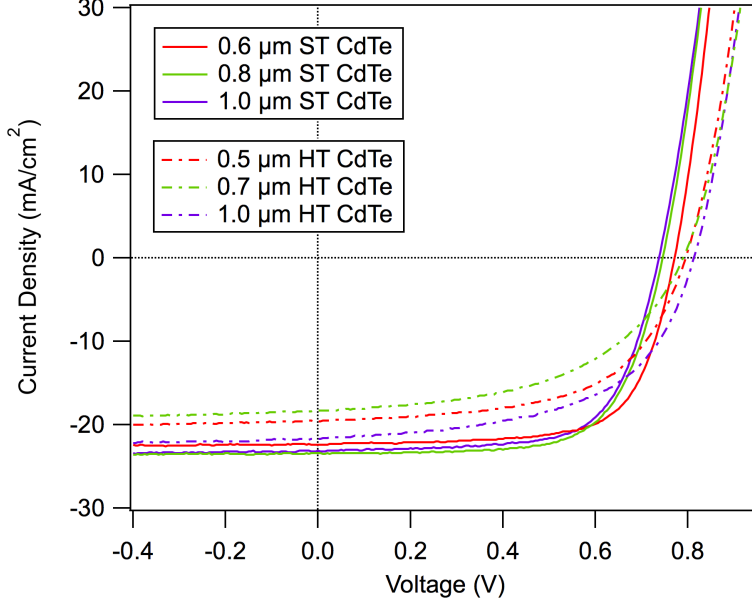


Fig. 5.1: Comparison of J-V curves of thin CdTe absorbers of similar thickness deposited at standard (ST) and high temperatures (HT). High deposition temperature leads to higher  $V_{OC}$  but lower fill factor.

To demonstrate the effects of voltage-dependent photocurrent, the total current density output by a CdTe solar cell can be represented as the difference between forward current,  $J_F(V)$ , and the voltage-dependent photocurrent,  $J_L(V)$  [32]:

$$J = J_F(V) - J_L(V) \quad (5.1)$$

where the forward current is defined by the standard diode equation with a correction for series resistance,  $R$ ,

$$J = J_0 \exp\left[\frac{q}{AkT}(V - RJ)\right] - J_{SC}. \quad (5.2)$$

Fig. 5.2 illustrates the effects of the voltage-dependent photocurrent on thin absorbers of various thicknesses, where  $J(V)$  is the measured J-V curve, and  $J_F(V)$  is calculated using values of  $R$  and  $A$  extracted from dark J-V curves. Devices with CdTe deposited at high temperature suffer from a large amount of voltage-dependent collection, which limits  $J_{SC}$  and fill factor values.

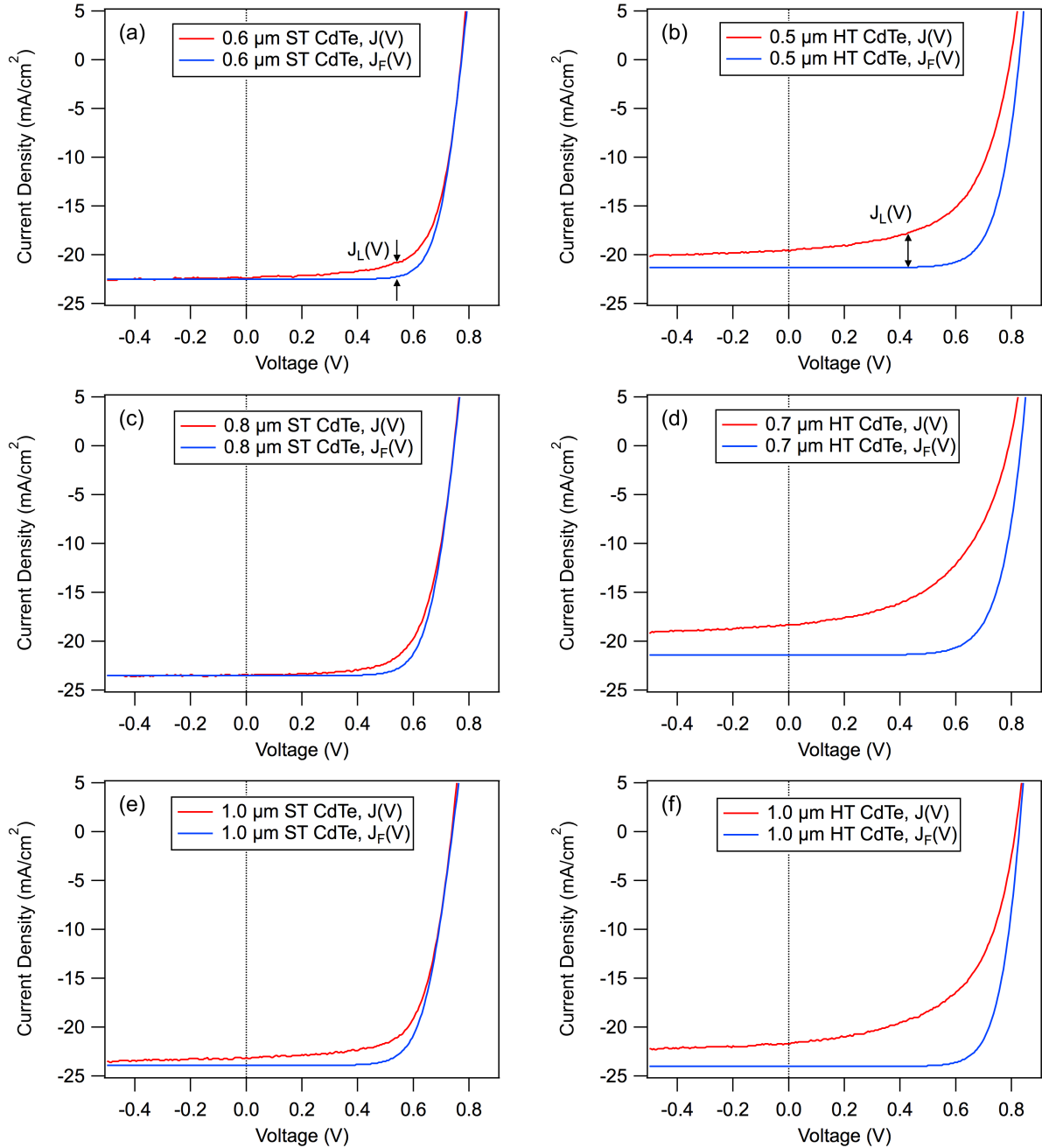


Fig. 5.2: Total current density,  $J(V)$ , and forward current density,  $J_F(V)$ , for devices of comparable CdTe thickness deposited at standard (ST) and high temperatures (HT). Higher deposition temperature leads to increased voltage-dependent collection,  $J_L(V)$ .

Additionally, modeling predicts voltage-dependent collection occurs in CdTe devices with high carrier concentrations and low carrier lifetimes [27]. This is supported by TRPL results in Fig. 5.3 which shows high deposition temperature leads to lower carrier lifetimes.

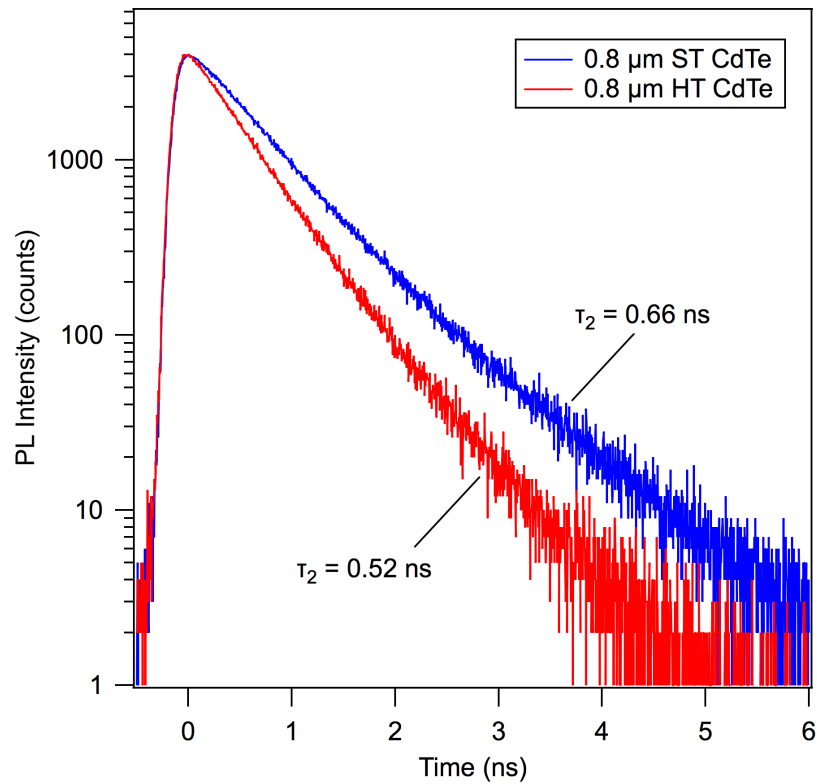


Fig. 5.3: TRPL results for 0.8  $\mu\text{m}$  CdTe devices deposited at standard (ST) and high temperatures (HT), measured from the glass side. Higher deposition temperatures leads to shorter minority carrier lifetimes. Credit: Darius Kuciauskas.

## 5.2 CdCl<sub>2</sub> Passivation

In order to determine the optimal passivation treatment for high temperature CdTe, a sweep of CdCl<sub>2</sub> dose was performed on devices with 1.0- $\mu\text{m}$  absorbers. Following the high temperature CdTe deposition, CdCl<sub>2</sub> was applied in varying doses followed by a constant annealing process at 400°C for 180 seconds. The dose times were 58, 78, 98, 118, 138, 158 and 180 seconds, and were selected based on the results of Section 4.1.1. The results of J-V characterization for high temperature CdTe are shown in Fig. 5.4.

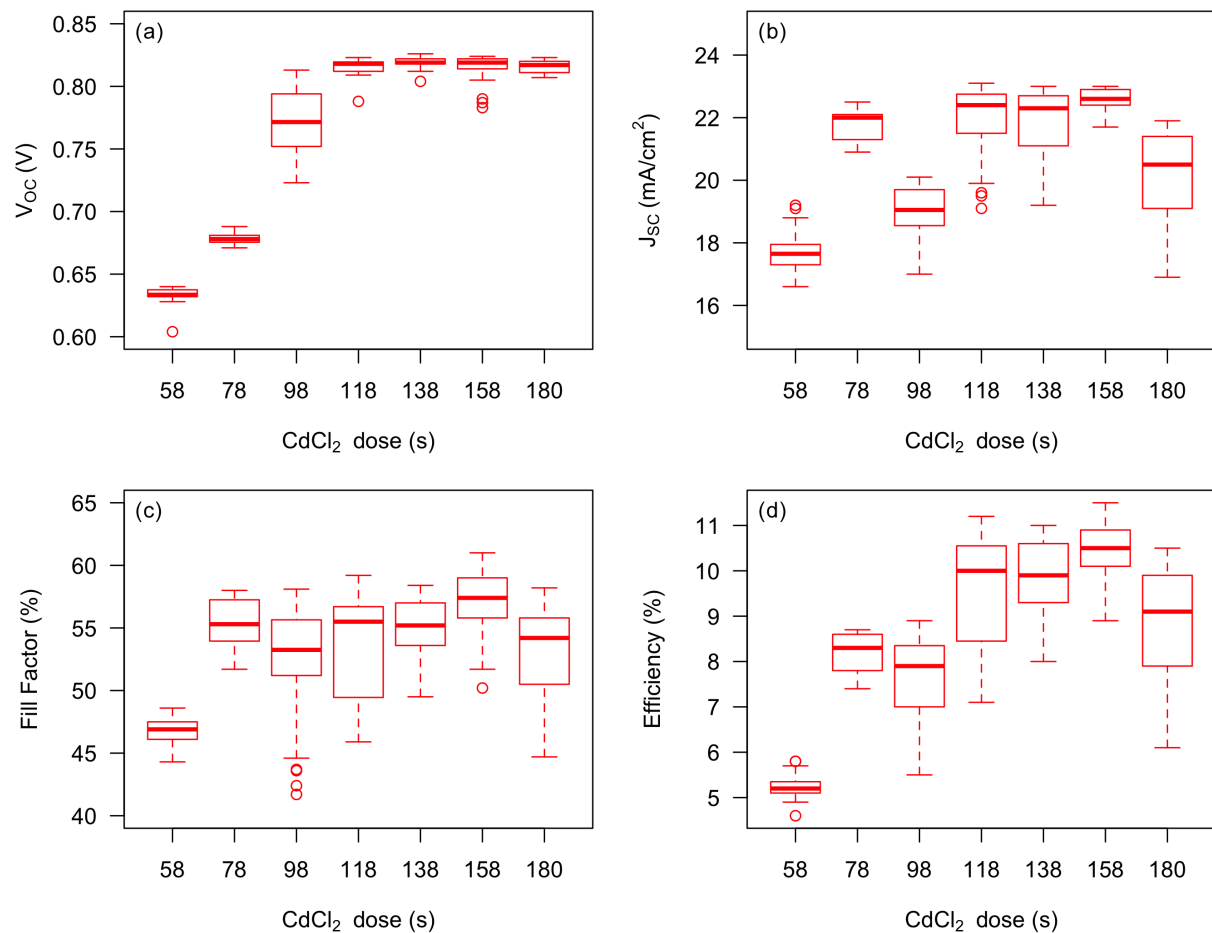


Fig. 5.4: J-V metrics as a function of CdCl<sub>2</sub> dose for devices with 1.0- $\mu\text{m}$  CdTe deposited at high temperature. ( $n = 13 - 19$  devices, some extreme outliers were removed)

Fig. 5.5 compares the top performing 1.0- $\mu\text{m}$  devices at each CdCl<sub>2</sub> dose time for both standard and high temperature. The benefit of larger grain formation is demonstrated

in Fig. 5.5(a) which shows that higher growth temperature produces consistently higher  $V_{OC}$  values. However, the fill factors for high temperature CdTe suffers considerably, a consequence of voltage-dependent collection and shorter carrier lifetimes.

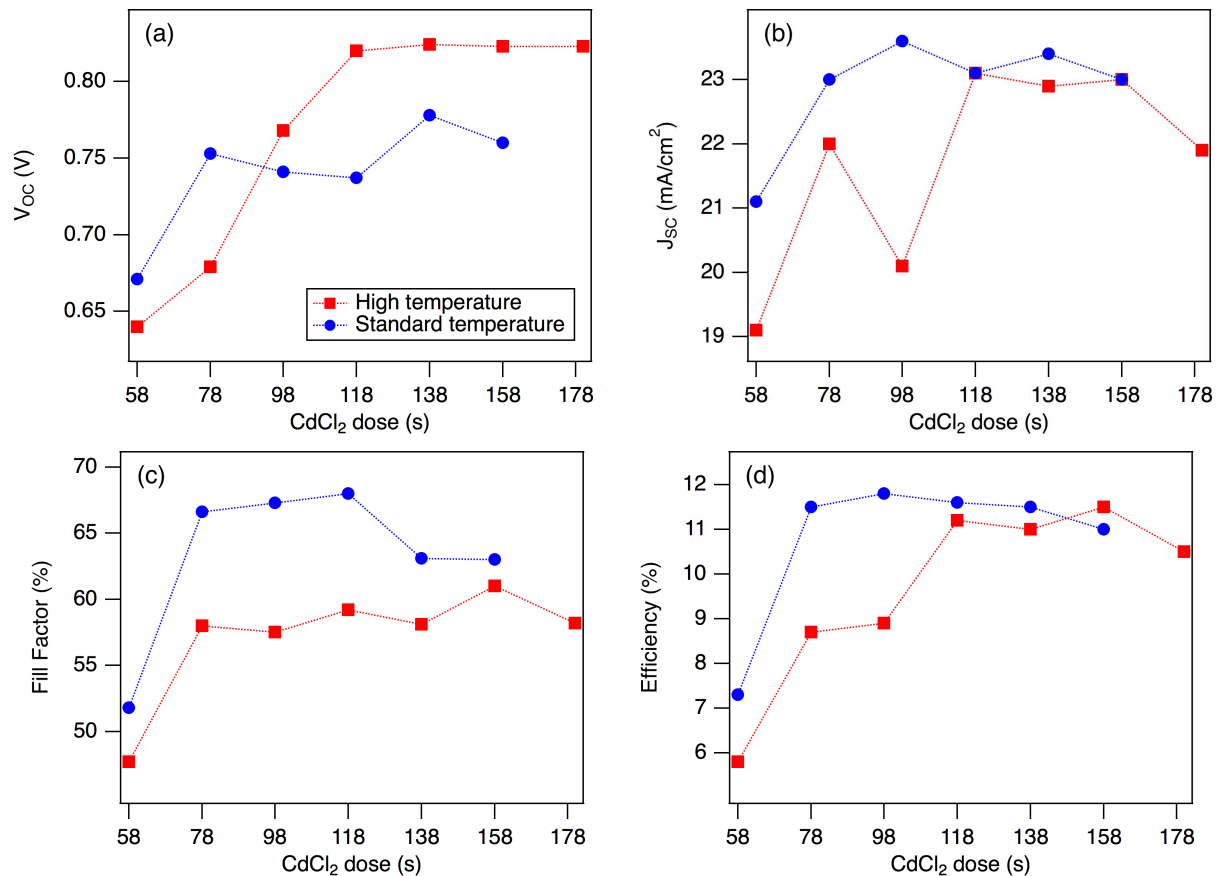


Fig. 5.5: J-V metrics as a function of CdCl<sub>2</sub> dose for top performing devices with 1.0- $\mu\text{m}$  CdTe grown at standard and high temperatures. The standard temperature data is taken from Section 4.1.1.

By looking at Fig. 5.5(d), we see standard temperature CdTe produces the best performing devices at lower CdCl<sub>2</sub> doses, while high temperature CdTe produces best performing devices at higher CdCl<sub>2</sub> doses. As high temperature deposition is known to lead to a Te-rich phase of CdTe with cadmium vacancies, the longer dose time required for high deposition temperature is consistent with the passivation of additional  $V_{Cd-Cl}$  complexes [33].

# Chapter 6

## CONCLUSIONS

With the increasing need to wean our dependence on fossil fuels, it becomes more important than ever for renewable energy sources such as solar PV to address existing technological issues. Until high recombination rates are addressed, CdTe remains unable to realize its full potential as one of the highest theoretical efficiency single-junction technologies today. A thin CdTe cell architecture was proposed as a means of reducing bulk recombination by fully extending the internal electric field to the back contact, thus creating separate conduction pathways for electrons and holes throughout the device. It was shown that thin CdTe devices are capable of being fully or near fully-depleted while unbiased.

In order to realize a thin CdTe solar cell, a basic routine for absorber post-deposition processing needed to be established. The optimal CdCl<sub>2</sub> and CuCl treatments were determined for 1.0 μm CdTe absorbers through experiments conducted via close-space sublimation. The results suggest thin CdTe absorbers require considerably less processing in general than standard thicker devices as expected.

Thin CdTe devices were found to be optimally passivated with approximately 120 to 140 seconds of CdCl<sub>2</sub> exposure followed by an annealing process of 120 seconds. The CdCl<sub>2</sub> treatment was discovered to be fairly flexible in both exposure and anneal time, as well as absorber thickness, producing comparable efficiencies of 11-12% for absorbers 0.6 μm to 1.2 μm thick.

Cu-doping experiments resulted in an optimal treatment of 2 seconds CuCl exposure followed by a 50 second annealing process. Devices with optimal copper treatment reached efficiencies of up to 13%. Cu-doping led to an increase in average  $V_{OC}$  from 790 to 840 mV and significantly improved device uniformity, however, also led to increased J-V crossover with longer CuCl exposure. Additionally, devices that were annealed for longer demonstrated

a significant drop in average fill factor from 68% to 54% with a simultaneous increase in parasitic effects and ideality factor, potentially indicating the diffusion of Cu atoms towards the junction.

The effects of CdTe growth temperature were also investigated. Devices with CdTe deposited at higher temperature lead to improved average  $V_{OC}$  values from about 750 to 800 mV consistent with larger grain formation, but also produced significant voltage-dependent collection resulting in large fill factor losses. Average fill factor decreased from 69% at lower deposition temperature to 55% at high deposition temperature for absorbers ranging 0.5 to 1.0  $\mu\text{m}$  in thickness. TRPL measurements showed high growth temperature also leads to lower carrier lifetimes, consistent with literature and the decrease in fill factor observed. Lastly,  $\text{CdCl}_2$  passivation of high temperature CdTe yielded an optimal dose time slightly longer than what was found for lower growth temperature. As high temperature CdTe is associated with Te-richness, this is consistent with an increase in Cd vacancies and Cd-based defect states requiring additional passivation.

Analysis of performance revealed that thin CdTe cells also suffer from unique optical and electrical losses not as prevalent in thicker devices. A comparison of current losses between of 0.6 and 1.0  $\mu\text{m}$  devices showed that the thinner device suffered an additional 2.1  $\text{mA}/\text{cm}^2$  of current loss. Of this, 1.0  $\text{mA}/\text{cm}^2$  was due to unabsorbed photons while the remaining 1.1  $\text{mA}/\text{cm}^2$  was attributed to increased recombination rates. TRPL results illustrated that thinner CdTe layers have shorter minority carrier lifetimes ranging 0.44 to 1.25 ns for absorbers 0.4 to 1.2  $\mu\text{m}$  thick, consistent with the increase in recombination observed for the thinner device. A fill factor loss analysis was also performed between 1.3 and 3.0  $\mu\text{m}$  CdTe devices. The results revealed that thin CdTe cells suffer additional fill factor losses due mostly to poor diode quality and some electrical shunting, accounting for an additional 7% (absolute) fill factor loss compared to the thicker device.

While thin CdTe cells have presented their own set of challenges, devices made at CSU have already produced efficiencies of up to 14.0% and demonstrated  $V_{OC}$  values near 850 mV.

Thinner CdTe devices seem especially susceptible to the recombination effects facilitated by short minority carrier lifetimes, however, it's been shown that sufficiently-thick devices of with absorbers  $\geq 1.0 \mu\text{m}$  are still capable of achieving good, reliable performance with carrier lifetimes close to 1 ns. With further improvements to the basic cell architecture, thin CdTe devices could potentially see even higher performance. Current on-going efforts entail adding an electron reflector which has been shown in models to successfully boost thin CdTe voltages. The expanded-bandgap electron reflector is an alloyed CdMgTe layer adjacent to the absorber which reduces back-surface recombination due to electron flow. In the future, use of an optical reflector may also become useful in mitigating current losses associated with thin CdTe transparency as well.

# Bibliography

- [1] E. Dlugokencky and P. Tans, “Trends in atmospheric carbon dioxide.” NOAA/ESRL, <https://www.esrl.noaa.gov/gmd/ccgg/trends/>, August 2017. Accessed: 08-15-2017.
- [2] T. M. Razykov, C. S. Ferekides, D. Morel, E. Stefanakos, H. S. Ullal, and H. M. Upadhyaya, “Solar photovoltaic electricity: Current status and future prospects,” *Solar Energy*, vol. 85, pp. 1580–1608, 2011.
- [3] M. Woodhouse, R. Jones-Albertus, D. Feldman, R. Fu, K. Horowitz, D. Chung, D. Jordan, and S. Kurtz, *On the Path to SunShot: The Role of Advancements in Solar Photovoltaic Efficiency, Reliability, and Costs*. National Renewable Energy Laboratory, 2016.
- [4] N. M. Haegel, R. Margolis, T. Buonassisi, D. Feldman, A. Froitzheim, R. Garabedian, M. Green, S. Glunz, H. Henning, B. Holder, I. Kaizuka, B. Kroposki, K. Matsubara, S. Niki, K. Sakurai, R. A. Schindler, W. Tumas, E. R. Weber, G. Wilson, M. Woodhouse, and S. Kurtz, “Terawatt-scale photovoltaics: Trajectories and challenges,” *Science*, vol. 365, pp. 141–143, 2017.
- [5] “Lazard levelized cost of energy analysis version 10.0.” <https://www.lazard.com/media/438038/levelized-cost-of-energy-v100.pdf>, December 2016. Accessed: 08-15-2017.
- [6] C. Helbig, A. M. Bradshaw, C. Kolotzek, A. Thorenz, and A. Tuma, “Supply risks associated with CdTe and CIGS thin-film photovoltaics,” *Applied Energy*, vol. 178, pp. 422–433, 2016.

- [7] T. A. Gessert, *Earth Systems and Environmental Sciences*, vol. 1, ch. Cadmium Telluride Photovoltaic Thin Film: CdTe, pp. 423–438. Elsevier, 2012.
- [8] M. A. Green, *Solar Cells: Operating Principles, Technology and System Applications*. University of South Wales, 1998.
- [9] D. A. Neamen, *Semiconductor Physics and Devices*. McGraw-Hill, 4th ed., 2012.
- [10] Wikipedia Commons, <https://commons.wikimedia.org/wiki/File:Pn-junction-equilibrium-graph.svg>, 2014. Accessed: 08-07-2016.
- [11] M. Boyd and C. Hansen, “Single diode equivalent circuit models.” PV Performance Modeling Collaborative, <https://pvpmc.sandia.gov/modeling-steps/2-dc-module-iv/diode-equivalent-circuit-models/>, 2014. Accessed: 08-07-2017.
- [12] B. McCandless and J. R. Sites, *Handbook of Photovoltaic Science and Engineering*, ch. Cadmium Telluride Solar Cells, pp. 617–662. John Wiley & Sons, 2003.
- [13] W. Shockley and H. J. Queisser, “Detailed balance limit of efficiency of p-n junction solar cells,” *Journal of Applied Physics*, vol. 43, pp. 510–519, 1961.
- [14] S. Ruhle, “Tabulated values of the Shockley-Queisser limit for single junction,” *Solar Energy*, vol. 130, pp. 139–147, 2016.
- [15] R. M. Geisthardt, M. Topič, and J. R. Sites, “Status and potential of CdTe solar-cell efficiency,” *IEEE Journal of Photovoltaics*, vol. 5, no. 4, pp. 1217–1221, 2015.
- [16] B. E. McCandless and K. D. Dobson, “Processing options for CdTe thin film solar cells,” *Solar Energy*, vol. 77, pp. 839–856, 2004.
- [17] C. Li, J. Poplawsky, Y. Yan, and S. J. Pennycook, “Understanding individual defects in CdTe thin-film solar cells via STEM: from atomic structure to electrical activity,” *Materials Science in Semiconductor Processing*, vol. 65, pp. 64–76, 2017.

- [18] S. S. Hegedus and B. E. McCandless, “CdTe contacts for CdTe/CdS solar cells: effect of Cu thickness, surface preparation and recontacting on device performance and stability,” *Solar Energy Materials & Solar Cells*, vol. 88, pp. 75–95, 2005.
- [19] K. D. Dobson, I. Visoly-Fisher, G. Hodes, and D. Cahen, “Stability of CdTe/CdS thin-film solar cells,” *Solar Energy Materials & Solar Cells*, vol. 62, pp. 295–325, 2000.
- [20] D. Swanson, J. Kephart, P. S. Kobayakov, K. Walters, K. C. Cameron, K. L. Barth, W. S. Sampath, J. Drayton, and J. R. Sites, “Single vacuum chamber with multiple close space sublimation sources to fabricate CdTe solar cells,” *Journal of Vacuum Science & Technology A: Vacuum, Surfaces, and Films*, vol. 34, 2016.
- [21] K. Hsiao, *Electron-Reflector Strategy for CdTe Thin-Film Solar Cells*. PhD thesis, Colorado State University, 2010.
- [22] S. S. Hegedus and W. N. Shafarman, “Thin-film solar cells: Device measurements and analysis,” *Progress in Photovoltaics: Research and Applications*, vol. 12, pp. 155–176, 2004.
- [23] M. Gloeckler, “CurVA software.” Colorado State University, 2005.
- [24] J. R. Sites and P. H. Mauk, “Diode quality factor determination for thin-film solar cells,” *Solar Cells*, vol. 27, pp. 411–417, 1989.
- [25] J. M. Raguse and J. R. Sites, “Correlation of electroluminescence with open-circuit voltage from thin-film CdTe cell,” *IEEE Journal of Photovoltaics*, vol. 5, no. 4, pp. 1175–1178, 2015.
- [26] U. Rau, “Reciprocity relation between photovoltaic quantum efficiency and electroluminescent emission of solar cells,” *Physical Review B*, vol. 76, 2007.

- [27] A. Kanevce and T. A. Gessert, "Optimizing CdTe solar cell performance: Impact of variations in minority-carrier lifetime and carrier density profile," *IEEE Journal of Photovoltaics*, vol. 1, pp. 99–103, 2011.
- [28] T. J. McMahon and A. L. Fahrenbruch, "Insights into the nonideal behavior of CdS/CdTe solar cells," *28th IEEE Photovoltaic Specialists Conference Proceedings*, pp. 539–542, 2000.
- [29] C. R. Corwine, A. O. Pudov, M. Gloeckler, S. H. Demtsu, and J. R. Sites, "Copper inclusion and migration from the back contact in CdTe solar cells," *Solar Energy Materials and Solar Cells*, vol. 82, pp. 481–489, 2004.
- [30] J. D. Major, Y. Y. Proskuryakov, K. Durose, G. Zoppi, and I. Forbes, "Control of grain size in sublimation-grown CdTe, and the improvement in performance of devices with systematically increased grain size," *Solar Energy Materials & Solar Cells*, vol. 94, pp. 1107–1112, 2010.
- [31] J. Ma, D. Kuciauskas, D. Albin, R. Bhattacharya, M. Reese, T. Barnes, J. V. Li, T. Gessert, and S.-H. Wei, "Dependence of the minority-carrier lifetime on the stoichiometry of CdTe using time-resolved photoluminescence and first-principles calculations," *Physical Review Letters*, vol. 111, no. 6, 2013.
- [32] S. S. Hegedus, S. Desai, and C. Thompson, "Voltage dependent photocurrent collection in CdTe/CdS solar cells," *Progress in Photovoltaics: Research and Applications*, vol. 5, pp. 587–602, 2007.
- [33] A. Rohatgi, "Study of efficiency limiting defects in polycrystalline CdTe/CdS solar cells," *International Journal of Solar Energy*, vol. 12, no. 1–4, pp. 37–49, 1992.